International Journal of Geo-Information

MDPI

Article

How Does the 2D/3D Urban Morphology Affect the Urban Heat Island across Urban Functional Zones? A Case Study of Beijing, China

Shouhang Du, Yuhui Wu *, Liyuan Guo, Deqin Fan and Wenbin Sun

College of Geoscience and Surveying Engineering, China University of Mining and Technology (Beijing), Beijing 100083, China; dush@cumtb.edu.cn (S.D.); sqt2300205106@student.cumtb.edu.cn (L.G.); deqinfan@cumtb.edu.cn (D.F.); swb@cumtb.edu.cn (W.S.)
* Correspondence: five139363@163.com

Abstract: Studying driving factors of the urban heat island phenomenon is vital for enhancing urban ecological environments. Urban functional zones (UFZs), key for planning and management, have a substantial impact on the urban thermal environment through their two-dimensional (2D)/three-dimensional (3D) morphology. Despite prior research on land use and landscape patterns, understanding the effects of 2D/3D urban morphology in different UFZs is lacking. This study employs Landsat-8 remote sensing data to retrieve the land surface temperature (LST). A method combining supervised and unsupervised classification is proposed for UFZ mapping, utilizing multi-source geospatial data. Subsequently, parameters defining the 2D/3D urban morphology of UFZs are established. Finally, the Pearson correlation analysis and GeoDetector are used to analyze the driving factors. The results indicate the following: (1) In the Fifth Ring Road area of Beijing, the residential zones exhibit the highest LST, followed by the industrial zones. (2) In 2D urban morphology, the percentage of built-up landscape (built-PLAND) and Shannon's diversity index (SHDI) are the main factors influencing LST. In 3D urban morphology, building density, the sky view factor (SVF), and the area-weighted mean shape index (shape index) are the main factors influencing LST. Therefore, low-density buildings with simple and dispersed shapes contribute to mitigating LST, while fragmented distributions of trees, grasslands, and water bodies also play important roles in alleviating LST. (3) In the interactive detection results, all UFZs show the highest interaction detection results with the built-PLAND. (4) Spatial variations are observed in the impact of different UFZs on LST. For instance, in the residential zones, industrial zones, green space zones, and public service zones, the SVF is negatively correlated with LST, while in the commercial zones, the SVF exhibits a positive correlation with LST.

Keywords: urban heat island; land surface temperature; urban functional zone; urban morphology; GeoDetector

Citation: Du, S.; Wu, Y.; Guo, L.; Fan, D.; Sun, W. How Does the 2D/3D Urban Morphology Affect the Urban Heat Island across Urban Functional Zones? A Case Study of Beijing, China. *ISPRS Int. J. Geo-Inf.* **2024**, *13*, 120. https://doi.org/10.3390/ijgi13040120

Academic Editors: Wolfgang Kainz, Jiangfeng She, Min Yang and Jun Zhu

Received: 23 January 2024
Revised: 26 March 2024
Accepted: 1 April 2024
Published: 4 April 2024

1. Introduction

In the process of urbanization, large-scale urban land development has become one of the primary ways in which human activities reshape the natural environment. One of the environmental impacts of urbanization is the phenomenon known as the urban heat island (UHI) effect, where the temperature in urban areas is higher than in the surrounding regions [1]. This effect is exacerbated by the rapid urbanization and widespread transition from natural landscapes to impervious surfaces, leading to increased absorption of solar radiation at the surface and reduced evapotranspiration from natural vegetation [2]. Furthermore, with the exacerbation of global warming, rapid urban expansion, and the increasing occurrence of extreme weather conditions, the UHI effect has significantly affected air quality, vegetation phenology, as well as the health and comfort of residents [3].

Consequently, mitigating the UHI effect has become a focal point of research in various related fields.

The UHI effect can be assessed through air temperature or land surface temperature (LST). While air temperature is primarily measured by meteorological stations, the limited and scattered nature of these stations provides only partial insights into urban temperature variations. LST results from the energy flux and interactions between the Earth and the atmosphere, playing a regulatory role in the lower atmospheric temperature of cities [4]. Scholars have conducted diverse studies on LST. For instance, Liu et al. utilized a three-step method, blending MODIS LST products and Landsat data to generate surface temperature for the summer months from 2003 to 2018. Their research revealed that the streets with high UHI effects in Beijing were mainly concentrated in the city center, while the streets with low UHI effects were predominantly in the suburbs [5]. Yang et al., using a single-window algorithm in conjunction with Landsat 8 TM10 band, performed LST inversion and found a close correlation between the surface temperature in Shanghai and the distribution of buildings [6]. David et al. investigated the relationship between simulated surface UHI (SUHI), thermal field variations, and land use indices. Their study identified the conversion of natural and agricultural land to urban or bare land as the primary cause of increased LST and SUHI [7]. With the continuous development of satellite remote sensing technology, various satellite images (e.g., Landsat, MODIS) can rapidly and accurately reflect differences in urban surface temperature and urban morphology, providing a foundational dataset for local climate studies [8]. Consequently, LST is widely employed to explore the relationship between the UHI effect and urban morphological indicators, such as land use/land cover types and landscape patterns [9,10].

Urban areas represent complex dynamic systems characterized by both two-dimensional (2D) and three-dimensional (3D) spatial features [11]. Previous research on factors influencing LST has predominantly focused on 2D urban spatial morphology, examining the impact of green spaces, water bodies, and impervious surfaces on LST [12]. Some studies have found that the impact of urban spatial morphology on LST is not always linear, but rather influenced by geographical location and seasonality [1,9,13]. This implies that there may be variations in LST response among different regions and seasons. Additionally, research indicates a positive correlation between building area, main road area, and the Normalized Difference Built-up Index (NDBI) with LST. Conversely, water body area and Normalized Difference Vegetation Index (NDVI) have been found to be negatively correlated with LST [14,15]. This suggests that water bodies and vegetation play significant roles in reducing LST. Although these studies have selected various indicators at different scales to explore the relationship between urban spatial morphology and LST, they have predominantly focused on 2D spatial morphology. In contrast, 3D morphological information is a crucial characteristic of urbanization, with buildings serving as key components of urban structure and major influencers of the UHI effect. This is because buildings can alter the reflection and absorption of solar radiation and the heat diffusion within urban areas [16].

With the acceleration of urbanization, the quantity and height of buildings in urban areas continue to rise, prompting researchers to focus on the relationship between the 3D spatial morphology of cities and LST. Factors such as building height, volume, density, and shape coefficient have been widely applied, and scholars have found significant correlations between these factors and LST [17,18]. As remote sensing technology continues to advance, an increasing number of scholars are contemplating the impact of both 2D and 3D urban morphology on LST. Research has found that both types of indicators influence LST. However, there is some controversy regarding whether 2D indicators or 3D indicators play a more significant role in shaping LST in urban areas. Alavipanah et al. argue that 3D indicators are more important in shaping the LST of different urban structures compared to 2D indicators [19]. However, Huang et al. suggest that the influence of 2D morphology on LST is superior to that of 3D morphology [20]. Therefore, empirical results regarding the impact of 2D and 3D urban environments on LST require further investigation.

In addition, many of these studies are based on entire cities, grids, or street units. For example, Koko et al. explored the relationship between land use/land cover changes and LST in Abuja, Nigeria. They found that LST is negatively correlated with NDVI and positively correlated with NDBI, indicating that urban expansion and reduced vegetation lead to increased LST [21]. Chen et al. investigated the relationship between LST and urban morphology in the core area of Xi'an at different grid scales. They identified average building height as a seasonally stable factor with a cooling effect [22]. Zhang et al. explored the relationship between LST and urban morphology in Beijing and Shanghai using streets as spatial units. They found that building density is the most important factor influencing LST, with 3D building forms being the most significant [1]. However, these approaches cannot fully characterize the basic spatial units of a city, warranting further exploration, based on finer spatial units, to investigate factors influencing the urban thermal environment.

In addition to land cover and surface geometry, urban morphology encompasses a variety of functional zones associated with various human activities. Urban functional zones (UFZs) are delineated based on different physical characteristics, as well as social and economic functions, and they often serve as fundamental units in urban planning [23]. Therefore, studying the 2D/3D urban morphology based on spatial units of UFZs holds greater practical significance for understanding the UHI effect. However, in the current literature, scholars have extensively studied the factors influencing LST at large scales, but there is a limited investigation into the influencing factors of LST at the finer scale of UFZs. Moreover, the intricate relationship between 2D and 3D urban morphology and LST requires a comparative analysis that considers 3D building features. This study aims to utilize multi-source geospatial data to more effectively represent the physical characteristics, as well as the social and economic functions within the study area, facilitating a fine-scale examination of the 2D/3D urban morphology's response to the UHI effect.

Due to rapid urbanization, Beijing, as a mega-city in China, experiences a significant UHI effect. This study seeks to leverage multiple sources of geospatial data to retrieve the LST in Beijing and create a map of UFZs. Using Pearson correlation analysis and GeoDetector, the study aims to investigate the relationship between 2D/3D urban morphology and the UHI effect in different UFZs. The analysis results of Beijing have significant implications for other cities. The specific objectives of this study are as follows: (1) to retrieve and analyze the distribution of LST in Beijing; (2) to investigate the distribution characteristics of UFZs in Beijing; (3) to explore the relationship between different types of UFZs and LST; and (4) to examine the relationship between the 2D and 3D urban morphology parameters of UFZs and LST.

2. Study Area and Dataset

2.1. Study Area

As the capital of China, Beijing stands as one of China's mega-cities, boasting the most developed and dynamic economy in the northern region. Characterized by a typical continental monsoon climate, Beijing experiences an average temperature of 12 °C, with annual precipitation ranging between 400–800 mm, unevenly distributed across seasons, with nearly 80% of rainfall concentrated in the summer. Since the late 1980s, Beijing has undergone significant urbanization, witnessing a remarkable demographic shift, from 9.043 million residents to 21.84 million as of 2022, as well as an expansion of the urban area from 346 square kilometers to 1469 square kilometers by 2022 [24]. The rapid expansion of the city has led to an increasingly prominent UHI effect in Beijing. The local climate and air quality further exacerbate the impact of this UHI effect. The central area within the Fifth Ring Road in Beijing, characterized by high levels of urbanization, encompasses a diverse range of commercial, residential, industrial, and public service zones. There are large rural areas surrounding the Fifth Ring Road of Beijing (Figure 1d). Different regions within this area exhibit distinct 2D and 3D urban morphologies, making it an ideal region for studying the UHI effect (Figure 1). Due to the relatively consistent climate and terrain within the study area, their impact on LST is not considered.

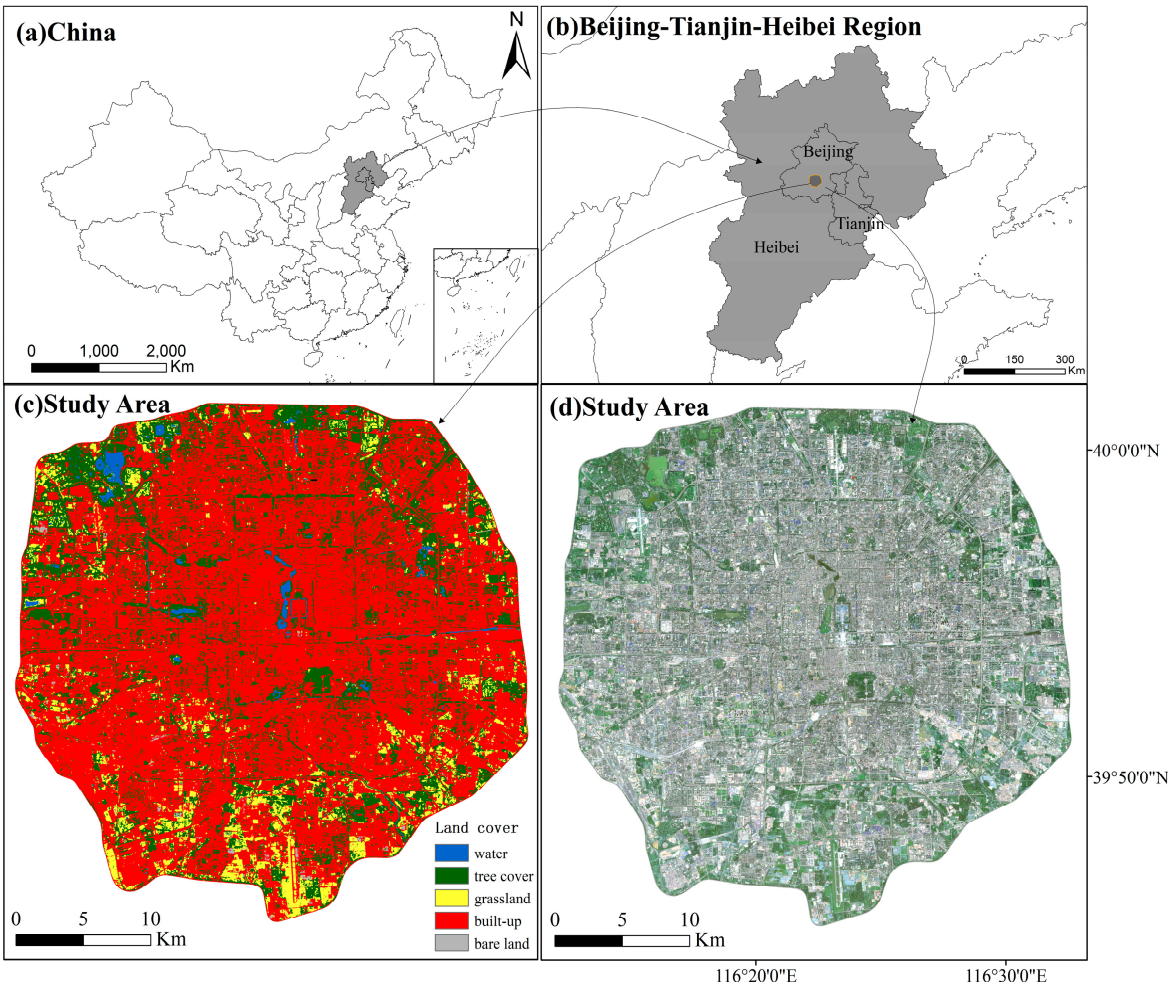

Figure 1. Study Area. (**a**) Beijing-Tianjin-Hebei region; (**b**) Fifth Ring Road of Beijing; (**c**) land cover map of the area within the Beijing Fifth Ring Road (data sourced from the European Space Agency: https://dataspace.copernicus.eu/ (accessed on 15 July 2023); (**d**) Sentinel-2 image.

2.2. Dataset

The data used in this study are mainly used to achieve LST inversion, UFZ mapping, and 2D/3D urban morphology calculations, as shown in Table 1.

The Operational Land Imager (OLI) carried by the Landsat 8 satellite comprises nine bands with a spatial resolution of up to 30 m, including a 15 m panchromatic band. The Landsat 8 OLI image, selected as the remote sensing data source, was employed for retrieving LST. Considering the collection time of urban Point of Interest (POI) data and the quality of remote sensing image, we obtained a total of two satellite images for the area within the Fifth Ring Road of Beijing from 1 August 2021 to 15 August 2021, using Google Earth Engine. One of the images was captured on 6 August 2021, with a cloud coverage of 3.06%. The other image was taken on 13 August, with a cloud coverage exceeding 5%, but the clouds did not cover the study area. All captures were during daylight hours. Subsequently, we processed the two images using Google Earth Engine to remove clouds, then merged them into a single image.

Luojia 1-01 successfully launched into orbit on 2 June 2018. With a ground resolution accuracy of 130 m, under ideal conditions, it can complete global nighttime image mapping within 15 days. Compared to earlier DMSP-OLS and NPP-VIIRS nighttime light data, the data from the Luojia 1-01 satellite offers higher spatial resolution advantageous for small-scale studies [25]. This study will utilize imagery from 23 November 2018.

Table 1. Data sources and descriptions.

Purpose	Data	Resolution	Time	Data Source
LST retrieval	Landsat-8	30 m	1 August 2021–15 August 2021	https://earthexplorer.usgs.gov/ (accessed on 15 July 2023)
	Luojia 1-01	130 m	2018	http://59.175.109.173:8888/app/login.html (accessed on 27 February 2024)
UFZ mapping	Sentinel-2	10 m	2022	https://dataspace.copernicus.eu/ (accessed on 17 July 2023)
	OSM	shp	2021	https://www.openstreetmap.org/ (accessed on 15 July 2023)
	POI	shp	2022	https://www.amap.com/ (accessed on 15 July 2023)
Accuracy assessment	Baidu Satellite Map	/	/	https://map.baidu.com/ (accessed on 15 July 2023)
2D factors calculation	WorldCover v200	10 m	2021.08.10	https://dataspace.copernicus.eu/ (accessed on 15 July 2023)
3D factors calculation	Building vectors	shp	2019	https://mp.weixin.qq.com/s/kCLLrSI7aPu7sSqi-Fuvhg (accessed on 14 July 2023)

Sentinel-2 is a high-resolution multispectral imaging mission under the European Space Agency's Copernicus program. This mission consists of two identical satellites, namely Sentinel-2A and Sentinel-2B, with a revisit period of 10 days for each satellite. The two satellites complement each other, resulting in a combined revisit period of 5 days [26]. In this study, Sentinel-2 images are utilized to calculate the NDVI (Normalized Difference Vegetation Index) and NDWI (Normalized Difference Water Index) within the Beijing Fifth Ring Road.

In this study, OpenStreetMap (OSM) road network and POI data were utilized to identify UFZs. Road network data were obtained from the official OSM website (https://www.openstreetmap.org/, accessed on 15 July 2023) [27]. The road network data include basic spatial information, such as latitude and longitude, as well as attribute information, such as road names, road types, maximum driving speeds, and one-way indicators. The study primarily retained the main road network, comprising highways, main roads, first-level roads, second-level roads, and third-level roads, to divide the study area into irregular units for UFZ mapping.

POI data were sourced from the Amap API open data platform (accessed in February 2022), including attributes such as POI names, geographic information, locations, and categories. The original POI data were intricate and contained redundancies. Some data did not effectively represent certain urban features, leading to low public acceptance. Therefore, facilities such as public toilets, ATMs, and cemeteries were excluded. Following the "Code for classification of urban and rural land use and planning standards of development land (GB50137)", the study area was categorized into residential zones, commercial zones, industrial zones, public service zones, and green spaces. After cropping and reclassification, a total of 558,333 POI points were used (Table 2).

The land cover data in this study utilized WorldCover v200 with a spatial resolution of 10 m. The WorldCover dataset, a collaborative effort of the European Space Agency and multiple global scientific research institutions, provides 10 m resolution land cover information. This dataset is generated based on data from Sentinel-1 and Sentinel-2 satellites. It encompasses 11 land cover categories and has undergone independent validation, with an overall global accuracy of approximately 75%. The land cover data for the year 2021 were employed in this study (Figure 1c). In addition, the building vector data comes from an open sharing platform.

Table 2. POI reclassification.

UFZ Categories	POI Categories	Number
Residential	Commercial and residential areas, residential areas, dormitories, villa areas, etc.	23,153
Commercial	Companies, catering, leisure and entertainment, gas stations, sports and fitness, shopping and consumption, banking, life services, etc.	478,751
Industrial	Factories, industrial parks	2310
Public service	Public utilities, medical care, science, education and culture, schools, libraries, etc.	52,383
Green space	Scenic spots, parks, tourist attractions, memorial halls, city squares, etc.	1736

3. Method

The workflow of this study is illustrated in Figure 2, encompassing four components:

(1) First, the extraction of LST within the Fifth Ring Road of Beijing was conducted using Landsat-8 remote sensing image.

(2) Second, using OSM road network data, we partitioned the urban area into basic units and conducted supervised and unsupervised identification of UFZs based on multi-source data and POI attributes.

(3) Third, the computation of 2D and 3D urban morphological factors for UFZs was carried out using land cover data and building vectors.

(4) Finally, analysis of the relationship between 2D/3D urban morphology and LST in UFZs was conducted using Pearson correlation analysis and GeoDetector.

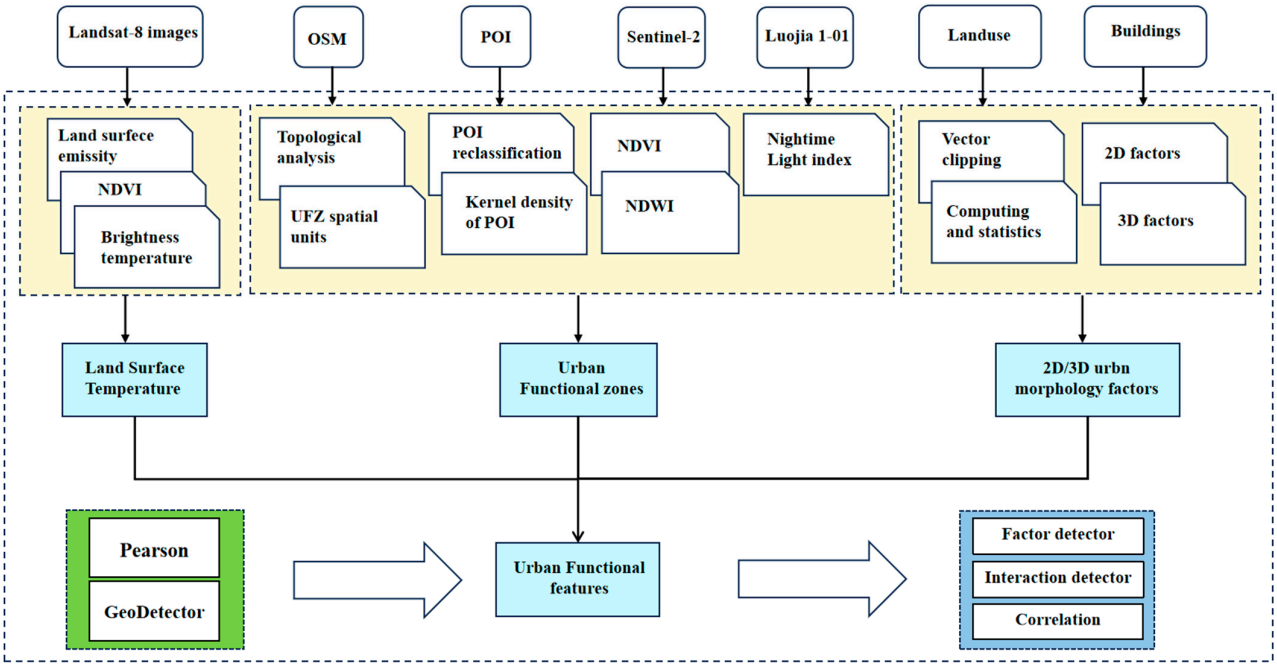

Figure 2. Workflow of this study.

3.1. LST Inversion

LST can be retrieved through various remote sensing sensors, such as MODIS and ASTER sensors, which are supported by the Terra and Aqua platforms [28], as well as the Landsat satellite series, supported by sensors like ETM, TM, and OLI. Landsat-8, with its higher spatial resolution and suitable spectral bands for the study area, was employed in this study for LST inversion [29]. Following the approaches of Feng et al. [30] and Huang et al. [20], an atmospheric correction method was applied to estimate the atmospheric

impact on LST radiation. To ensure robust results, this study selected summer images for inversion, given that the UHI effect is more pronounced during this season. Therefore, using the Google Earth Engine platform, the average of LST inversion results from 1 August 2021 to 15 August 2021 was calculated. The computation of LST in this study is described as follows:

$$L_\lambda = [\varepsilon B(T_S) + (1-\varepsilon)L_d]\tau + L_\mu \quad (1)$$

In the equations, L_λ represents the top-of-atmosphere (TOA) atmospheric radiance; ε denotes the surface emissivity; $B(T_S)$ signifies the thermal radiance derived from the Planck law at temperature t; τ is the transmissivity of the atmosphere in the thermal infrared band; and L_d and L_μ are the atmospheric downwelling and upwelling radiance, respectively. The relationship between $B(T_S)$ and L_λ can be expressed as follows:

$$B(T_S) = \frac{L_\lambda - L_\mu - \tau(1-\varepsilon)L_d}{\tau\varepsilon} \quad (2)$$

Thus, the LST (T_S) can be inverted from the Planck formula as follows:

$$T_s = \frac{K_2}{ln(K_1/B(T_S)+1)} \quad (3)$$

For Landsat-8, the constants are K_1 = 774.89 W/(m·sr·μm) and K_2 = 1321.08 K.

3.2. UFZ Mapping

For UFZ mapping, this study proposes a two-stage method that combines both unsupervised and supervised classification to leverage the strengths of various data sources. Prior to UFZ classification, we initiated topological processing of OSM road network data. On this basis, correction of interruptions and duplicate routes was performed, establishing a fundamental framework for the classification of independent units of UFZs.

In the first stage, a Sentinel-2 image was initially utilized to compute the NDVI and NDWI values. Thresholds were then set to distinguish green areas and water bodies, respectively. Subsequently, the total area proportion of green areas and water bodies within each UFZ was calculated. Based on these proportions, green space zones were determined, as they typically have a larger proportion of green areas and water bodies. Next, the average nighttime light index for each UFZ was computed, and a threshold was set to identify commercial zones, as these zones typically exhibit higher levels of luminosity at night. Commercial and green space zones were extracted in this step. Following this, a supervised classification approach was employed to identify the types of the remaining UFZs.

In the second stage, the remaining UFZs were classified using multi-source features and a random forest classifier. We utilized multiple data sources as features for each UFZ, including the average values of NDVI, NDWI, nighttime light index, and five normalized kernel density estimates of POI measures. However, the quantity of POIs varies across different types, with commercial POIs outnumbering others. This results in an imbalanced distribution of point numbers among different POI types [31]. To address these issues, we calculated the normalized kernel density of POI within each unit to determine UFZs. The function is expressed by the following formulas:

$$f(x) = \frac{1}{nh}\sum_{i=1}^{n} k\left(\frac{x-x_i}{h}\right) \quad (4)$$

$$F_{norm} = \frac{f(x) - f_{min}(x)}{f_{max}(x) - f_{min}(x)} \quad (5)$$

where $f(x)$ represents the kernel density function; $k\left(\frac{x-x_i}{h}\right)$ is the kernel function; n is the number of known points; h is the bandwidth; and $x - x_i$ is the distance from the grid center point to the known point. In Equation (5), F_{norm} is the normalized value of POI kernel

density, and $f_{min}(x)$ and $f_{max}(x)$ are the minimum and maximum values of POI kernel density, respectively.

The categories of certain UFZs were determined through manual visual interpretation, along with the green spaces and commercial zones identified in the first stage, serving as the training dataset for the random forest classifier to identify the remaining UFZs. In this study, the dataset is randomly divided into a training set (comprising 70% of the data) and a testing set (30% of the data). Random forest was trained on the training set and evaluated on the testing set. The random forest algorithm integrates predictions from multiple decision trees, effectively reducing the risk of overfitting [32].

To evaluate the accuracy of the proposed method, this study employed overall accuracy (OA) and Kappa coefficient metrics [33]. OA represents the ratio of correctly classified samples to the total number of samples, while Kappa is used to assess the consistency between classification results and actual categories. The calculation formula for OA is as follows:

$$\mathrm{OA} = \frac{\sum_{i=1}^{m} a_{ii}}{n} \tag{6}$$

where m represents the number of UFZ categories, a_{ii} denotes the number of correctly classified samples in each UFZ category, and n represents the total number of UFZ samples.

The calculation of OA is given by:

$$P_e = \frac{\sum_{i=1}^{m} a_i b_i}{n} \tag{7}$$

$$\mathrm{Kappa} = \frac{\mathrm{OA} - P_e}{1 - P_e} \tag{8}$$

where P_e represents the chance-corrected agreement, m denotes the number of UFZ categories, a_i signifies the actual number of samples in each UFZ category, and b_i represents the number of samples misclassified into each category.

3.3. 2D/3D Urban Morphology Factors

Patches are fundamental units composing landscape patterns, representing relatively homogeneous non-linear areas distinct from the surrounding background [34]. This study explored the relationship between the patchiness of land cover types and LST concerning UFZs, utilizing landscape metrics.

As shown in Table 3, 2D urban morphology encompasses surface cover landscape indices, while 3D urban morphology involves building forms computed through architectural calculations. Three widely used landscape indices were employed in this study to assess urban landscape patterns: percentage of landscape area (PLAND), patch density (PD), and Shannon's diversity index (SHDI). These indicators, calculated using FRAGSTATS 4.2, describe urban morphology from three perspectives: area proportion, shape complexity and diversity, and spatial arrangement. They effectively capture the ecological environment formed by the interaction of natural and anthropogenic factors within a region. Both PLAND and PD were calculated based on each land cover element, while SHDI was computed across all categories.

In addition, to focus on 3D architectural structures, six indices were constructed using building vectors, including the area-weighted mean shape index (shape index), building density (density), shape coefficient, mean height, height variance, and sky view factor (SVF). These six indicators encompass aspects of shape, composition, and distribution (Table 3). Buildings represent the primary aspects of 3D urban morphology, and the selected indices cover differences in building height, shape, density, and other horizontal and vertical dimensions. They comprehensively measure the 3D morphology within UFZs. The calculation of the SVF is conducted using the UMEP plugin in QGIS software 3.16. Figure 3 illustrates the building heights and SVF in a sample area. Considering the fact that the climate factors and the terrain factors are relatively consistent in the study area, this

study only discusses the influence of 2D/3D urban morphological parameters on daytime urban LST.

Table 3. 2D/3D urban morphology factors.

Type	Factor	Equation		Description
2D urban morphology factors	Percentage of landscape (PLAND)	$PLAND = \frac{\sum_{j=1}^{n} a_{ij}}{A} \times 100$	a_{ij} represents the area of the *j*-th patch in the *i*-th landscape type; A is the total area of the landscape	Describe the proportion of the land type in the landscape
	Patch density (PD)	$PD = \frac{NP}{A}$	NP is the number of patches; A is the total area of the landscape or patches	Describe the number of patches per unit area; the greater the density of patches, the finer the granularity of the landscape
	Shannon's diversity index (SHDI)	$SHDI = -\sum P_i \ln P_i$	P_i is the proportion of species *i* in the total number of species	Describe the complexity and variability of patches in the landscape; when there is only one patch type in the landscape, SHDI = 0
	Area-weighted mean shape index (shape index)	Shape index $= \frac{C}{\sqrt{S}}$	C is the perimeter of the patches, S is the area of the patches	Shape complexity of individual buildings It is equal to the perimeter of the patch divided by the square root of the area of the patch
3D urban morphology factors	Density	$Density = \frac{\sum_{j=1}^{n} S_{ij}}{\sum_{i=1}^{n} S_i}$	S_{ij} represents the area of the *j*-th building in the *i*-th functional zone	Indicates the building density within each block
	Shape coefficient	Shape coefficient $= \frac{S}{V}$	S is the building surface area; V is the building volume	The ratio between exterior surface and building volume; it measures a building's ability to exchange heat with the surrounding environment
	Mean height	Mean height $= \frac{\sum_{i=1}^{n} h_i}{n}$	h_i is the height of the *i*-th building	Represents the average height of buildings in each block
	Height variance	Height variance $= \frac{\sum_{i=1}^{n} (h_i - MH)^2}{n}$	h_i is the height of the *i*-th building; MH is the average height of the building	Represents the height change of buildings within each block
	Sky view factor (SVF)	$SVF = 1 - \frac{\sum_{i=1}^{n} \sin\gamma_i}{n}$	γ_i represents the azimuth size of building height relative to the center, r, and n represents the number of azimuths within the buffer zone	The proportion of the covered hemisphere occupied by the sky, ranging from 0 (no sky visible) to 1 (no horizon obstruction visible); it measures the extent of a 3D open space

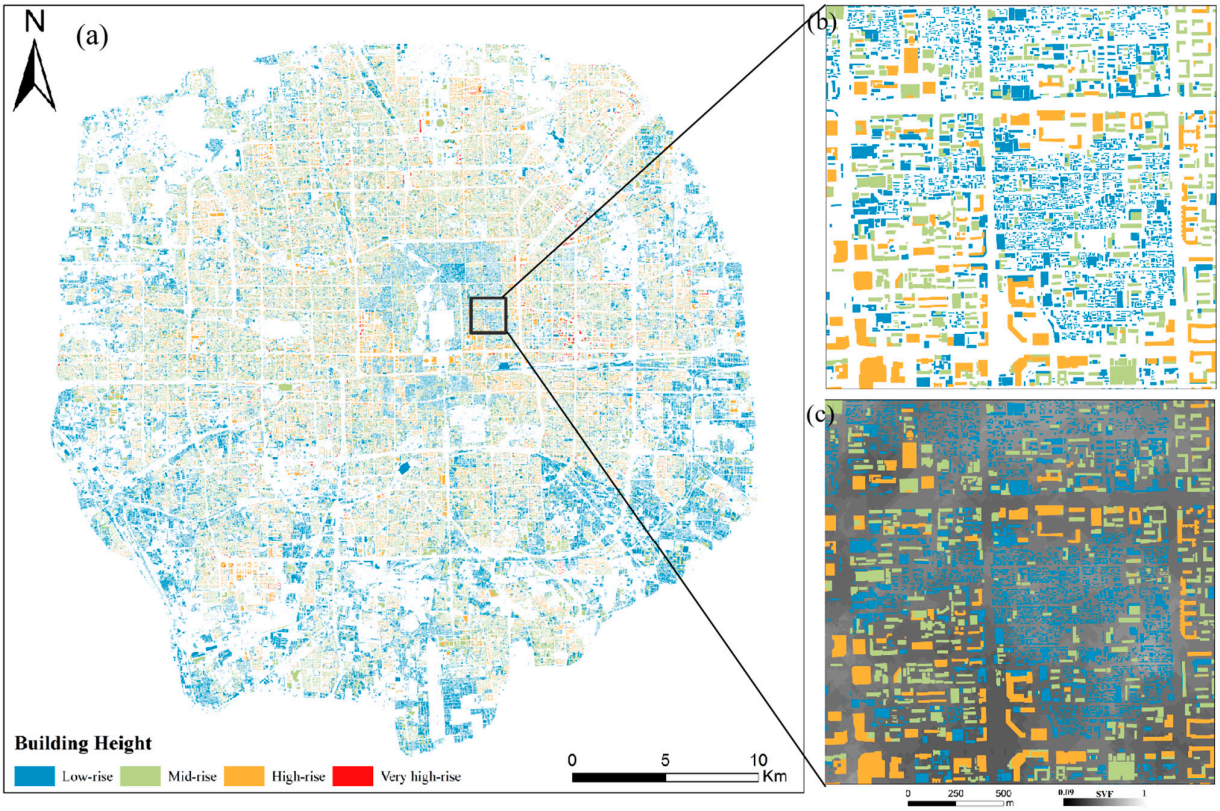

Figure 3. (**a**) Building height distribution within the Fifth Ring Road in Beijing. According to the "Chinese Civil Building Design Code", buildings are divided into four categories: low-rise (<10 m), mid-rise (10–24 m), high-rise (24–90 m) and super high-rise (>90 m). (**b**) Building height of a sample area and (**c**) SVF.

3.4. Data Analysis Methods

Using machine learning models may introduce the risk of overfitting, especially with limited sample sizes. In contrast, Pearson correlation analysis and GeoDetector are simpler and more suitable for our research purposes. Additionally, they can provide direct relationships and the extent of influence among indicators, making the results easy to interpret and understand. Therefore, this study will first employ Pearson correlation analysis to identify variables that may have significant effects. Subsequently, variables will be input into the GeoDetector model to analyze the relationship between urban morphology parameters and LST. In addition, these two methods have been successfully applied in the related field [20,35].

3.4.1. Pearson Correlation Analysis

Considering the potential correlation between 2D/3D urban morphology indicators and LST, this study employed Pearson correlation analysis to investigate the relationship between 2D/3D urban morphology indicators and LST. Pearson correlation analysis is a statistical method used to measure the strength and direction of the linear relationship between two variables. It is based on the concept of covariance, calculated by dividing the covariance of two variables by the product of their respective standard deviations, resulting in a correlation coefficient ranging from −1 to 1 [36]. The Pearson correlation formula is as follows:

$$r = \frac{\sum_{i=1}^{n}(x_i - \overline{x})(y_i - \overline{y})}{\sqrt{\sum_{i=1}^{n}(x_i - \overline{x})^2}\sqrt{\sum_{i=1}^{n}(y_i - \overline{y})^2}} \quad (9)$$

where x_i represents 2D/3D urban morphology indicators, y_i represents LST, and n is the sample size. The correlation coefficient ranges from −1 to 1: when $r > 0$, it indicates

a positive correlation between LST and the factor; when r < 0, it indicates a negative correlation; when r = 0, it indicates no correlation between LST and the factor.

3.4.2. GeoDetector

GeoDetector represents a set of statistical methods used to explore spatial variations and reveal the driving forces behind them. Its core concept is based on the assumption that if a certain independent variable significantly influences a dependent variable, their spatial distributions should exhibit similarity [37]. In this study, the differentiation and factor detection module of GeoDetector is employed to assess the explanatory power of the influencing factors on the spatial variation of LST in UFZs, as indicated by the formula:

$$q = 1 - \frac{\sum_{h=1}^{L} N_h \sigma_h^2}{N\sigma^2} \quad (10)$$

where q represents the explanatory power of a certain influencing factor on the spatial variation of LST in UFZs; h = 1,2,3,. . .; L denotes the layers of LST or influencing factors; N_h and N represent the number of units in layer h and the total number of UFZs, respectively; σ_h and σ^2 denote the variance of feature values in layer h and UFZs, respectively. The q value ranges from [0, 1], where a higher value indicates a stronger explanatory power of each influencing factor on the spatial variation of LST in UFZs [38].

The interaction detection module is employed to detect the types of interactions between the independent variables (X_i), determining whether the combination of different factors affects the explanatory power of the dependent variable (Y). This method first calculates the q value for each influencing factor and then computes the q value for each pair of factors after interaction, as presented in Table 4. A higher q value indicates a stronger joint explanatory power of the two factors [37].

Table 4. Interaction types.

Interaction Type	Judgments Based
Nonlinear weaken	$q(x_1 \cap x_2) < \min[q(x_1), q(x_2)]$
Single factor nonlinear weaken	$\min[q(x_1), q(x_2)] < q(x_1 \cap x_2) < [q(x_1), q(x_2)]$
Bivariate enhance	$q(x_1 \cap x_2) > \max[q(x_1), q(x_2)]$
Independent	$q(x_1 \cap x_2) = q(x_1), q(x_2)$
Nonlinear enhance	$q(x_1 \cap x_2) > q(x_1), q(x_2)$

4. Results

4.1. Results of UFZ Mapping

This study delineated 998 UFZs (Figure 4). Through analyzing normalized POI density, Baidu satellite images, and original images obtained from Baidu street view, combined with our understanding of the study area, we visually interpreted the categories of 236 UFZs. Along with the 64 green spaces and commercial zones identified in the first stage, a total of 300 UFZs were utilized for model training and accuracy assessment. The dataset was randomly divided into a training set, comprising 70% of the data, and a testing set, comprising 30% of the data. Finally, a confusion matrix was created, and the Kappa coefficient was calculated to determine the accuracy of the UFZ classification against the testing set. The overall accuracy of UFZ mapping in this study is 89%, with a Kappa coefficient of 0.85 (Figure 5). As depicted in Figure 5, based on the confusion matrix results, the correct recognition rates for the five UFZs are all above 80%. Specifically, residential zones had a 3.3% chance of being misclassified as commercial zones, 2.2% as industrial zones, 1.1% as green spaces, and 1.1% as public service zones. Commercial zones had a 3.4% chance of being misclassified as residential zones, 2.9% as green spaces, and 5.7% as public service zones. Industrial zones have had a 1.1% chance of being misclassified as residential zones, 5.9% as commercial zones. Green spaces had a 12.5% chance of being

misclassified as public service zones. Public service zones had a 5.9% chance of being misclassified as industrial zones, and a 3.2% chance of being misclassified as green spaces.

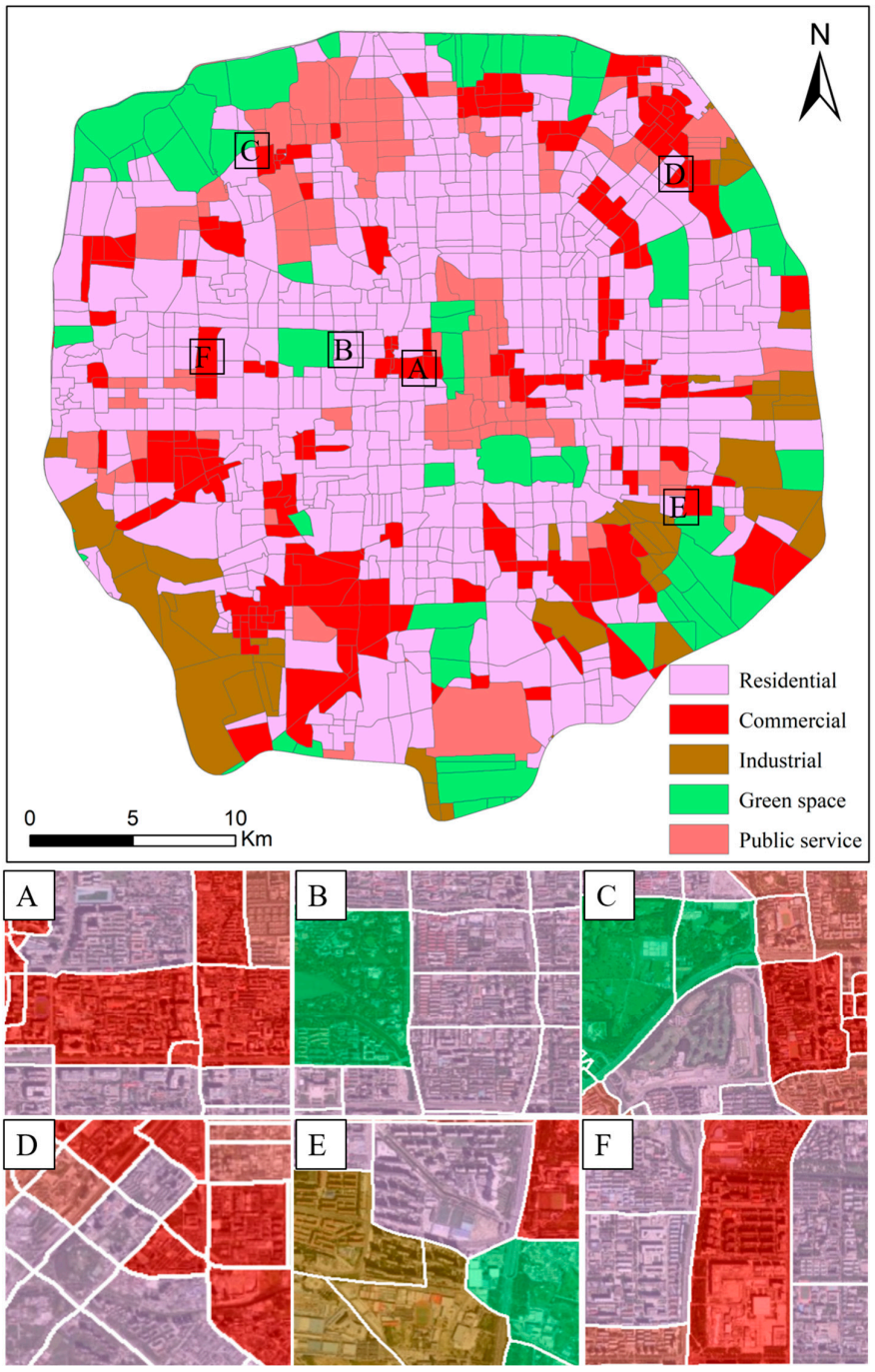

Figure 4. UFZ mapping results.

As shown in Table 5, a statistical analysis of UFZs types within the Fifth Ring Road of Beijing revealed 566 units were classified as residential zones, covering a total area of 573.48 km^2, constituting 45.4% of the total. There are 196 units classified as commercial zones, with a total area of 194.92 km^2, representing 15.4% of the total. Industrial zones comprised 57 units, covering a total area of 70.79 km^2, accounting for 5.6% of the total. Green spaces encompassed 72 units, with a total area of 328.90 km^2, making up 26% of the total. Public service land zones comprised 107 units, with a total area of 95.21 km^2, constituting 15.4% of the total.

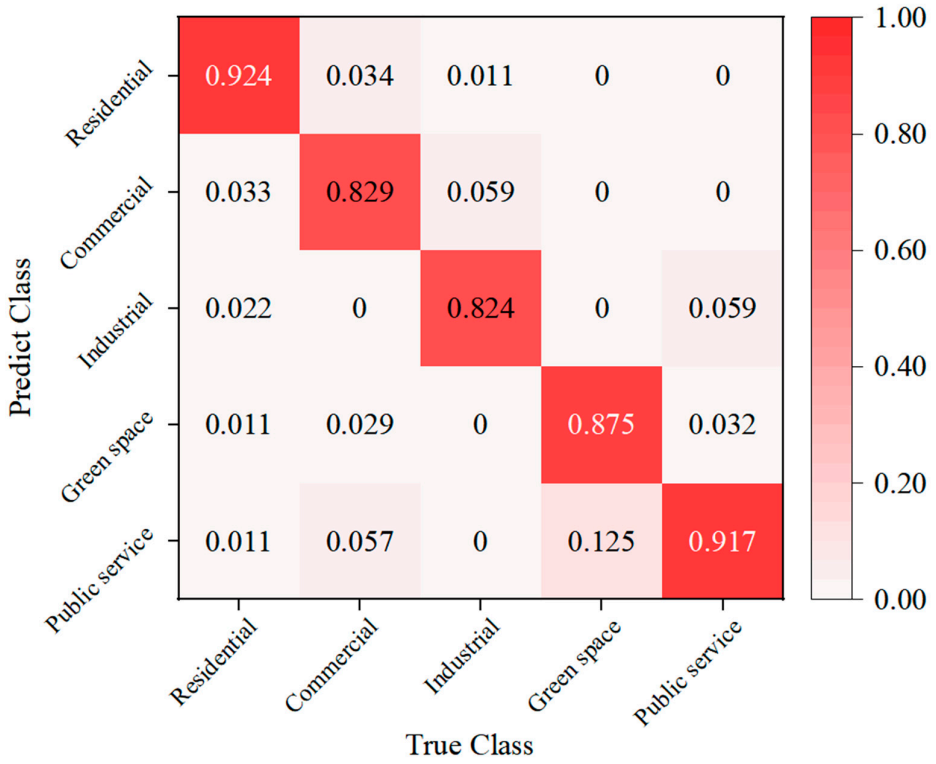

Figure 5. Accuracy evaluation of UFZ mapping results.

Table 5. UFZ statistics.

UFZs	Number	Total Area/km^2	Average Area/km^2
Residential	566	573.48	1.01
Commercial	196	194.92	0.99
Industrial	57	70.79	1.24
Green space	72	328.90	4.56
Public service	107	95.21	0.83
Total	998	1263.31	1.27

4.2. LST Inversion Results

The results of LST inversion reveal that the urban LST within the Fifth Ring Road of Beijing ranges from 25.65 °C to 40.85 °C (Figure 6), exhibiting an overall pattern of "high in the center, low in the periphery". As Beijing's urban area continues to expand, extensive buildings, roads, and artificial land cover the original landscape. These structures and roads absorb solar radiation energy and release it in the form of heat, causing an increase in temperature within the city. Consequently, the LST within the Fifth Ring Road of Beijing exhibits a central high-temperature pattern surrounded by lower temperatures.

Overlaying the LST with UFZs and utilizing the natural breaks method, the LST of UFZs is classified into five categories: low temperature (≤29.85 °C), sub-low temperature (29.86–30.70 °C), medium temperature (30.71–31.43 °C), sub-high temperature (31.44–32.10 °C), and high temperature (≥32.11 °C). As shown in Figures 7 and 8, the LST within the UFZs ranges from 28.23 °C to 33.44 °C. Residential zones and industrial zones exhibit higher LST, measuring 31.35 °C and 31.18 °C, respectively. The proportion of high temperatures in residential zones is 20.49%, while in industrial zones, it is 10.53%. Following closely are public service zones and commercial zones, with an LST of 31.16 °C and 31.12 °C, respectively. The proportions of high temperatures are 12.15% in public service zones and 13.27% in commercial zones. Green spaces have the lowest average LST, at 29.86 °C, with a high-temperature proportion of only 4.17%. According to Figure 9, industrial zones have the largest standard deviation, at 0.95 °C, while commercial zones

have the smallest one, at 0.87 °C. The research results indicate that residential zones have the highest LST, followed by industrial zones, while green spaces exhibit the lowest LST.

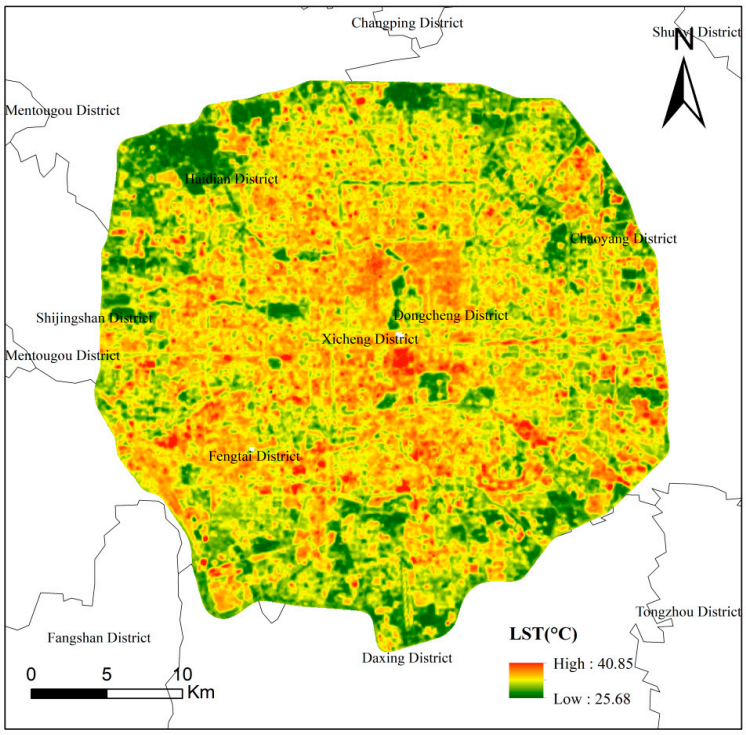

Figure 6. LST inversion results within the Fifth Ring Road in Beijing.

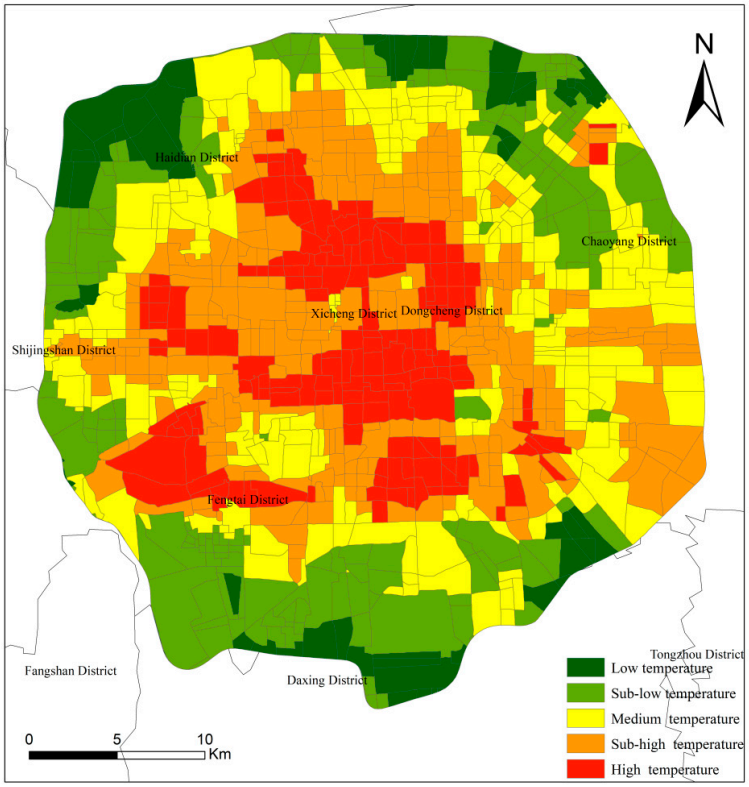

Figure 7. LST of different UFZs (low temperature (≤29.85 °C), sub-low temperature (29.86–30.70 °C), medium temperature (30.71–31.43 °C), sub-high temperature (31.44–32.10 °C), high temperature (≥32.11 °C)).

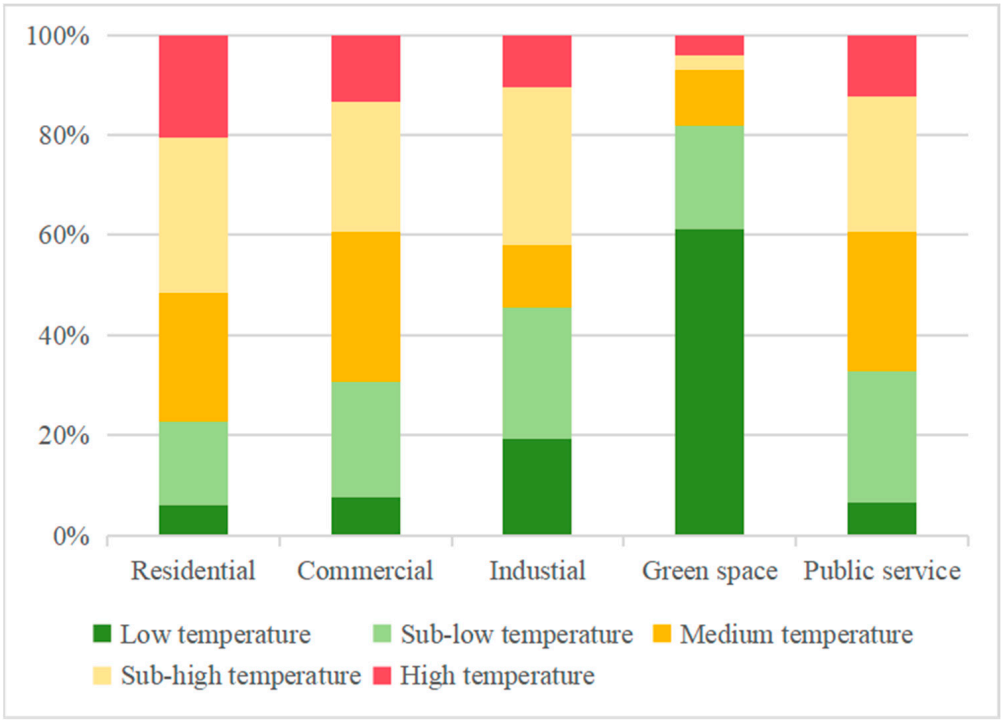

Figure 8. LST distribution of UFZs.

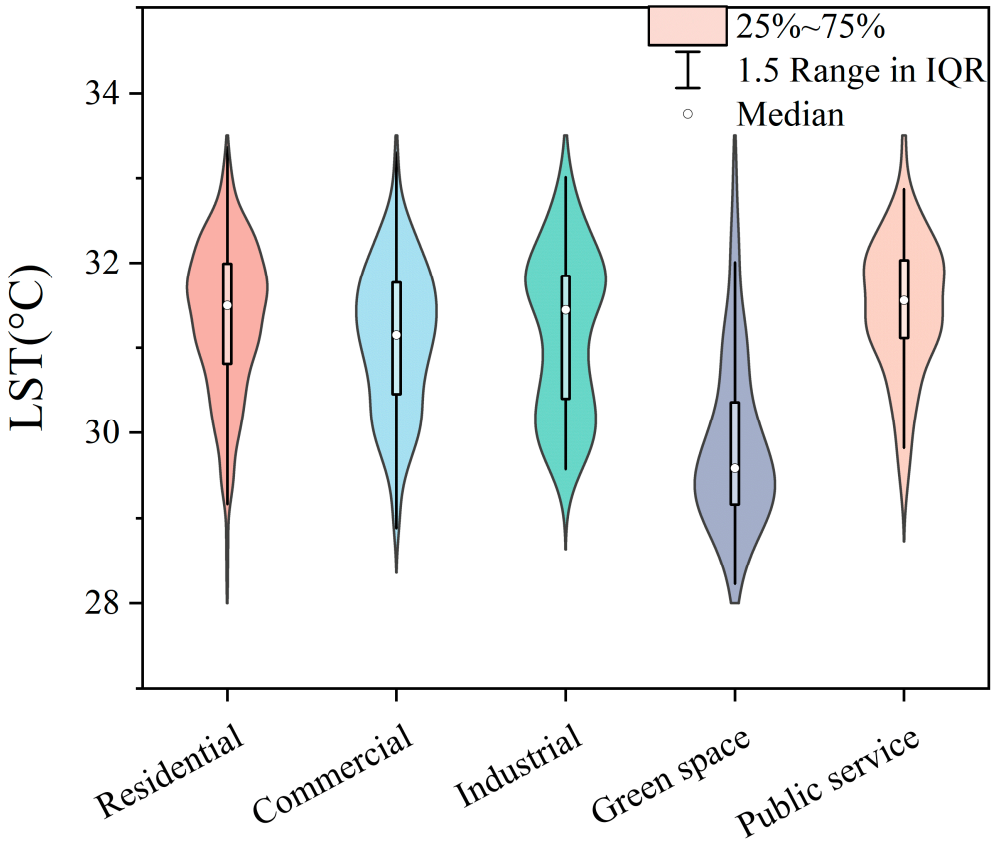

Figure 9. Violin plot and box plot of LST in UFZs (the white point is the middle value, the middle rectangle represents the mean value, the box limits represent the upper and lower quartiles, respectively, the box error bar represents the range within 1.5 IQR, and the black line shows distribution of data).

4.3. Factors Influencing Analysis

4.3.1. Correlation between 2D/3D Factors and LST

In terms of the impact of 2D urban morphological indicators on the LST of UFZs (Table 6), built-PLAND, built-PD, and SHDI in all five UFZs show significant correlations at the 1% significance level. Among them, all UFZs exhibit the highest positive correlation with built-PLAND, followed by relatively high negative correlations with SHDI and built-PD. This indicates that concentrated distribution of buildings, and uneven distribution of patches in the five UFZs may lead to an increase in LST. Moreover, grass, trees, and water show negative correlations with LST, suggesting that a higher proportion and dispersed distribution of trees and water within UFZs can effectively mitigate LST, while bare land shows a positive correlation with LST, indicating that fragmented bare land can lead to temperature increases.

Table 6. Pearson correlation coefficients between 2D factors and LST of UFZs.

	Residential	Commercial	Industrial	Green Space	Public Service
SHDI	−0.734 **	−0.706 **	−0.769 **	−0.758 **	−0.679 **
Built-up					
Built-PLAND	0.86 **	0.813 **	0.866 **	0.901 **	0.866 **
Built-PD	−0.451 **	−0.415 **	−0.417 **	−0.462 **	−0.463 **
Grass					
Grass-PLAND	−0.037	−0.1	−0.338 *	−0.087	−0.249 **
Grass-PD	−0.129 **	−0.172 *	−0.174	−0.034	−0.342 **
Tree					
Tree-PLAND	−0.2 **	−0.197 **	−0.473 **	−0.462 **	−0.062
Tree-PD	−0.228 **	−0.212 **	−0.422 **	−0.455 **	−0.143
Bare					
Bare-PLAND	0.165 **	0.108	0.402 **	0.225	0.146
Bare-PD	0.188 **	−0.115	0.434 **	0.258 *	0.140
Water					
Water-PLAND	−0.116 **	−0.236	−0.187	−0.173	−0.144
Water-PD	−0.138 **	−0.173	−0.239	−0.164	−0.146

* $p < 0.05$ (2-tailed). ** $p < 0.01$ (2-tailed).

Regarding the impact of 3D urban morphological indicators on the LST of UFZs (Table 7), building density shows the highest correlation in all UFZs and passes the 1% significance level test, with correlation coefficients of 0.566, 0.443, 0.412, 0.482, and 0.608, respectively. In addition, in all UFZs, the mean height shows a negative correlation with LST, indicating that taller buildings are more conducive to reducing LST. In residential zones, the shape index (r = 0.38, $p < 0.01$) and the SVF (r = −0.216, $p < 0.01$) suggest that simple and dispersed building shapes help alleviate LST. In the commercial zones, the shape index (r = 0.339, $p < 0.01$) and the height variance (r = −0.128) indicate that simpler building shapes and greater height variance contribute to lowering LST. In the industrial zones, the SVF (r = −0.409, $p < 0.01$) and the mean height (r = −0.401, $p < 0.01$) suggest that dispersed and taller buildings help mitigate LST. In green space zones, the shape index (r = 0.415, $p < 0.01$) and the SVF (r = −0.395) indicate that complex and dense building shapes may lead to higher LSTs. In public service zones, the shape index (r = 0.426, $p < 0.01$) and the SVF (r = −0.278, $p < 0.05$) indicate that complex and dense building shapes may lead to higher LSTs. Through comparing different UFZs, spatial variations in the impact on LST are observed. For instance, in the residential zones, industrial zones, green space zones, and public service zones, the SVF shows a negative correlation with LST, while in the commercial zones, the SVF is positively correlated with LST. Additionally, in the industrial zones and green space zones, height variance is positively correlated with LST, whereas in the residential zones, commercial zones, and public service zones, height variance exhibits a negative correlation with LST, with the industrial zones and green space zones showing a greater impact than the other three UFZs. Due to the strong correlation found between

2D/3D urban morphology parameters and LST in the Pearson correlation analysis, both 2D and 3D urban morphology parameters will be included in the subsequent analysis using GeoDetector.

Table 7. Pearson correlation coefficients between 3D factors and LST of UFZs.

	Residential	Commercial	Industrial	Green Space	Public Service
Shape index	0.38 **	0.339 **	0.186	0.415 **	0.426 **
Density	0.566 **	0.443 **	0.412 **	0.482 **	0.608 **
Shape coefficient	−0.025	0.096	−0.212	−0.021	0.267 **
Mean height	−0.212 **	−0.114	−0.401 **	−0.36 **	−0.023
Height variance	−0.132 **	−0.128	0.344 **	0.307 **	−0.016
SVF	−0.216	0.017	−0.409 **	−0.395	−0.278 *

* $p < 0.05$ (2-tailed). ** $p < 0.01$ (2-tailed).

4.3.2. The Influence of 2D/3D Factors on LST

From the perspective of the impact of 2D urban morphology factors on the LST of UFZs (Table 8), the built-PLAND exhibits the highest explanatory power, followed by the SHDI, for the LST in the five UFZs. The built-PLAND, grass-PLAND, tree-PLAND, and SHDI for the residential zones, commercial zones, industrial zones, public service zones, and green spaces are all significant at the 1% level. When considering individual UFZs for residential zones, all factors, except for water-PD, are significant at the 1% level, indicating a complex set of factors influencing the LST in the residential zones. In the commercial zones, built-PLAND (q = 0.558, $p < 0.01$), grass-PLAND (q = 0.357, $p < 0.01$), and SHDI (q = 0.481, $p < 0.01$) have a high explanatory power for LST spatial variability, suggesting a close correlation with these factors in the commercial zones. In the industrial zones, the built-PLAND (q = 0.777, $p < 0.01$), built-PD (q = 0.357, $p < 0.01$), and SHDI (q = 0.652, $p < 0.01$) have high explanatory power for the LST spatial variability. In the green spaces, except for bare soil and water bodies, all factors have high explanatory power for LST spatial variability. In the public service zones, the built-PLAND, built-PD, and SHDI have high explanatory power for the LST spatial variability, with all q values greater than 0.3 and being significant at the 1% level. Overall, among the 2D urban morphology indicators, built-PLAND and SHDI are identified as the primary factors influencing urban LST.

Table 8. The impact of 2D factors on LST across UFZs (PLAND and PD are denoted as "land cover -landscape index", where, for example, built-PLAND represents the PLAND of built-up area and built-PD represents the PD of the built-up area).

Factors	Residential	Commercial	Industrial	Green Space	Public Service
SHDI	0.543 **	0.481 **	0.652 **	0.643 **	0.473 **
Built-up					
Built-PLAND	0.740 **	0.558 **	0.777 **	0.865 **	0.787 **
Built-PD	0.388 **	0.219 **	0.357 **	0.325	0.376 **
Grassland					
Grass-PLAND	0.415 **	0.357 **	0.244 **	0.415 **	0.097 **
Grass-PD	0.329 **	0.256 **	0.240 **	0.363 *	0.195 **
Tree cover					
Tree-PLAND	0.273 **	0.248 **	0.321 **	0.267 **	0.134 **
Tree-PD	0.267 **	0.076 **	0.317 *	0.262 *	0.118 **
Bare					
Bare-PLAND	0.067 **	0.087 *	0.138	0.169	0.021
Bare-PD	0.065 **	0.093 *	0.111	0.071	0.075
Water					
Water-PLAND	0.022 **	0.053 **	0.062 *	0.041	0.043
Water-PD	0.018	0.040	0.047 *	0.039	0.067

* $p < 0.05$ (2-tailed). ** $p < 0.01$ (2-tailed).

In order to provide a clearer and more intuitive understanding of the impact of 2D/3D factors on the LST within different UFZs, we calculated the percentage of influence of 2D/3D factors in individual UFZs. This facilitates a comparison of their influence across different UFZs, as shown in Figures 10 and 11. Figure 10 illustrates a comparative analysis of the influence of various 2D factors within different types of UFZs. Among the five UFZs, SHDI and built-PLAND have the most significant impact on LST. In residential, commercial, and industrial zones, the influence of SHDI and built-PLAND on LST is generally similar. However, in green spaces and public service zones, the influence of built-PLAND exceeds that of SHDI. It is worth noting that in public service zones, the influence of built-PLAND on LST is the most significant. Additionally, compared to other UFZs, the impact of tree-PLAND and tree-PD on green spaces is more pronounced.

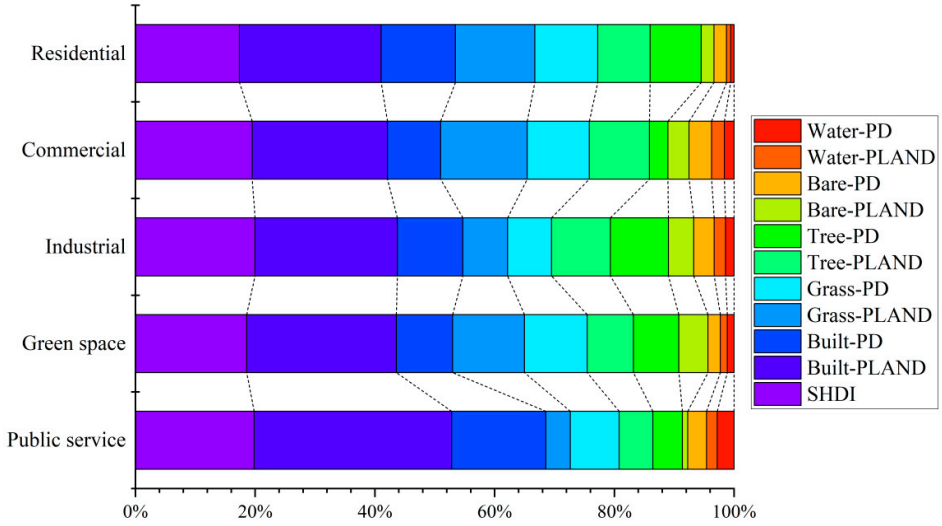

Figure 10. Differences in the influence degree of 2D factors on different UFZs.

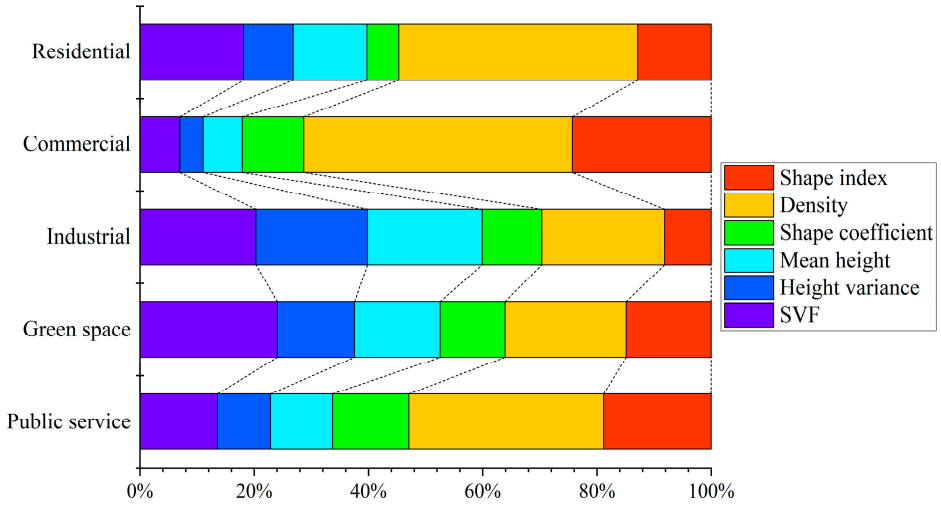

Figure 11. Differences in the influence degree of 3D factors on different UFZs.

Examining the impact of 3D urban morphological factors on the LST of UFZs (Table 9), the density values for the residential zones, commercial zones, industrial zones, green spaces, and public service zones are all significant at the 1% level, with q values of 0.521, 0.323, 0.467, 0.388, and 0.467, respectively. Specifically, for the residential zones, all four factors of 3D urban morphology have explanatory power for LST, passing the 1% significance test. Notably, the SVF (q = 0.226, $p < 0.01$) and the mean height (q = 0.161, $p < 0.01$) exhibit stronger explanatory power for spatial variations in LST in the residential

zones, indicating a close correlation between the residential zone LST and building height and sky visibility. In commercial zones, all 3D urban morphology factors are significant at the 1% level, except for height variance, and its explanatory power (q = 0.028) is the weakest. The shape index (q = 0.167, $p < 0.01$), the shape coefficient (q = 0.074, $p < 0.01$), and the SVF (q = 0.048, $p < 0.05$) demonstrate strong explanatory power for spatial variations in the LST in commercial zones, suggesting a close relationship between commercial zone LST and building shape and sky visibility. For the industrial zones, all the six factors of 3D urban morphology fail to pass the 1% significance test, except for density. However, the SVF (q = 0.441, $p < 0.05$) and the mean height (q = 0.436, $p < 0.05$) exhibit relatively stronger explanatory power for spatial variations in the LST in the industrial zones. In the green spaces, only the SVF and the shape index pass the 5% significance test, with the SVF (q = 0.44, $p < 0.05$), the shape index (q = 0.272, $p < 0.05$) and the mean height (q = 0.274) demonstrating stronger explanatory power for spatial variations in LST in the green spaces. For public service zones, only the shape coefficient and height variance failed the significance test, and although the shape coefficient has a q value of 0.183, it does not pass the 1% significance test. Overall, among the 3D urban morphology factors, density, SVF, and shape index are identified as the primary factors influencing urban LST.

Table 9. The impact of 3D factors on LST across UFZs.

Factors	Residential	Commercial	Industrial	Green Space	Public Service
Shape index	0.160 **	0.167 **	0.177 *	0.272 *	0.258 **
Density	0.521 **	0.323 **	0.467 **	0.388 **	0.467 **
Shape coefficient	0.069 **	0.074 **	0.227 *	0.208	0.183
Mean height	0.161 **	0.047 **	0.436 *	0.274	0.149 **
Height variance	0.108 **	0.028	0.424	0.247	0.127
SVF	0.226 **	0.048 *	0.441 *	0.44 *	0.186 *

* $p < 0.05$ (2-tailed). ** $p < 0.01$ (2-tailed).

As shown in Figure 11, among the five UFZs, density emerges as the primary factor influencing LST. Its impact is consistently prominent in commercial and residential zones, surpassing that of industrial zones, green spaces, and public service zones. The shape index significantly affects LST in commercial and public service zones. Meanwhile, the SVF demonstrates notable effects in residential, industrial, and green space zones. In industrial zones, aside from the shape index and shape coefficient, the remaining 3D urban factors exhibit similar impacts on LST.

4.3.3. Factor Interaction Analysis

Furthermore, the internal composition of UFZs is complex, and the influence on LST is also intricate. Investigating a single factor may not adequately characterize the relationship between them. Therefore, a dual-factor analysis was chosen to explore whether there is a stronger connection between the double factors and LST. The results of the interaction detection of the 3D urban morphological factors using GeoDetector (Figure 12) demonstrate that the interactive detection results of 3D factors in UFZs are both higher than the explanatory power of single factors. Moreover, they exhibit either bivariate enhancement or nonlinear enhancement, with no instances of mutual independence or weakening.

For the residential zones, the interaction strength between density and the mean height is 0.640, and the interaction strength between density and the shape index is q = 0.627. In the commercial zones, the interaction strength between density and the mean height is the same as the interaction strength between density and the shape index, both being q = 0.412. In the industrial zones, the interaction strength between density and the height variance is the highest (q = 0.765), followed by the interaction strength between density

and the mean height (q = 0.760). In the green spaces, the interaction strength between density and the mean height is the highest (q = 0.726), and the interaction strength between density and the shape index is the second highest (q = 0.724). For the public service zone, the interaction strength between density and the height variance is the highest (q = 0.782), followed by the interaction strength between the mean height and density (q = 0.764). The results indicate that the interaction between density and the mean height exhibits stronger explanatory power. Building density affects urban spatial layout, shape index is associated with individual building complexity, while mean height is correlated with airflow. Thus, the interaction between density, shape index, and mean height demonstrates the maximum explanatory power for LST, aligning well with the actual situation.

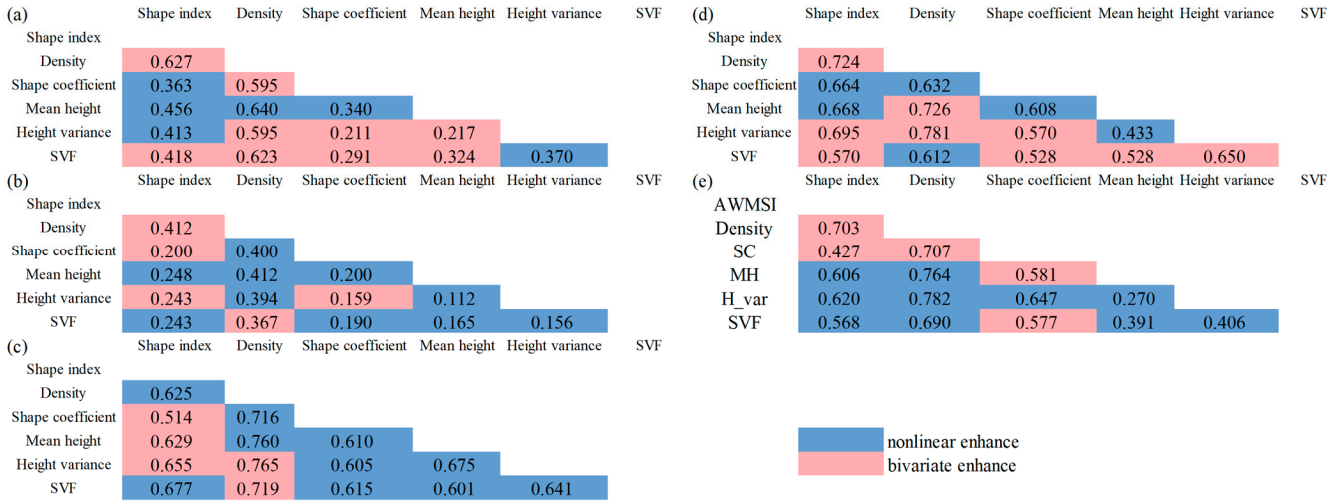

Figure 12. Three-dimensional factor interaction detection results in UFZs ((**a**) residential zone; (**b**) commercial zone; (**c**) industrial zone; (**d**) green space; (**e**) public service zone).

Through GeoDetector, the interactive detection results of various 2D landscape factors in UFZs were obtained (Figure 13). The results of the interactive detection of 2D factors are all greater than the explanatory power of single factors, and they exhibit either bivariate enhancement or nonlinear enhancement, with no instances of mutual independence or weakening.

In the residential zones, the highest interactive explanatory power is between the built-PLAND and built-PD (q = 0.798), followed by the interaction between built-PLAND and bare-PLAND (q = 0.787). In the commercial zones, the highest interactive explanatory power is between the built-PLAND and grass-PD (q = 0.644), followed by the interaction between built-PLAND and bare-PD (q = 0.622). In the industrial zones, the highest interactive explanatory power is between the built-PLAND and built-PD (q = 0.886), followed by the interaction between built-PD and SHDI (q = 0.901). In the green spaces, the highest interactive explanatory power is between the built-PLAND and built-PD (q = 0.948), followed by the interaction between built-PLAND and grass-PD (q = 0.936). For the public service zones, the highest interactive explanatory power is between the built-PLAND and built-PD (q = 0.890), followed by the interaction between built-PLAND and SHDI (q = 0.862).

Through GeoDetector, the interactive detection results of 2D/3D urban morphological factors in UFZs were obtained (Figure 14). The results of the interactive detection are all greater than the explanatory power of single factors, and they exhibit either bivariate enhancement or nonlinear enhancement, with no instances of mutual independence or weakening.

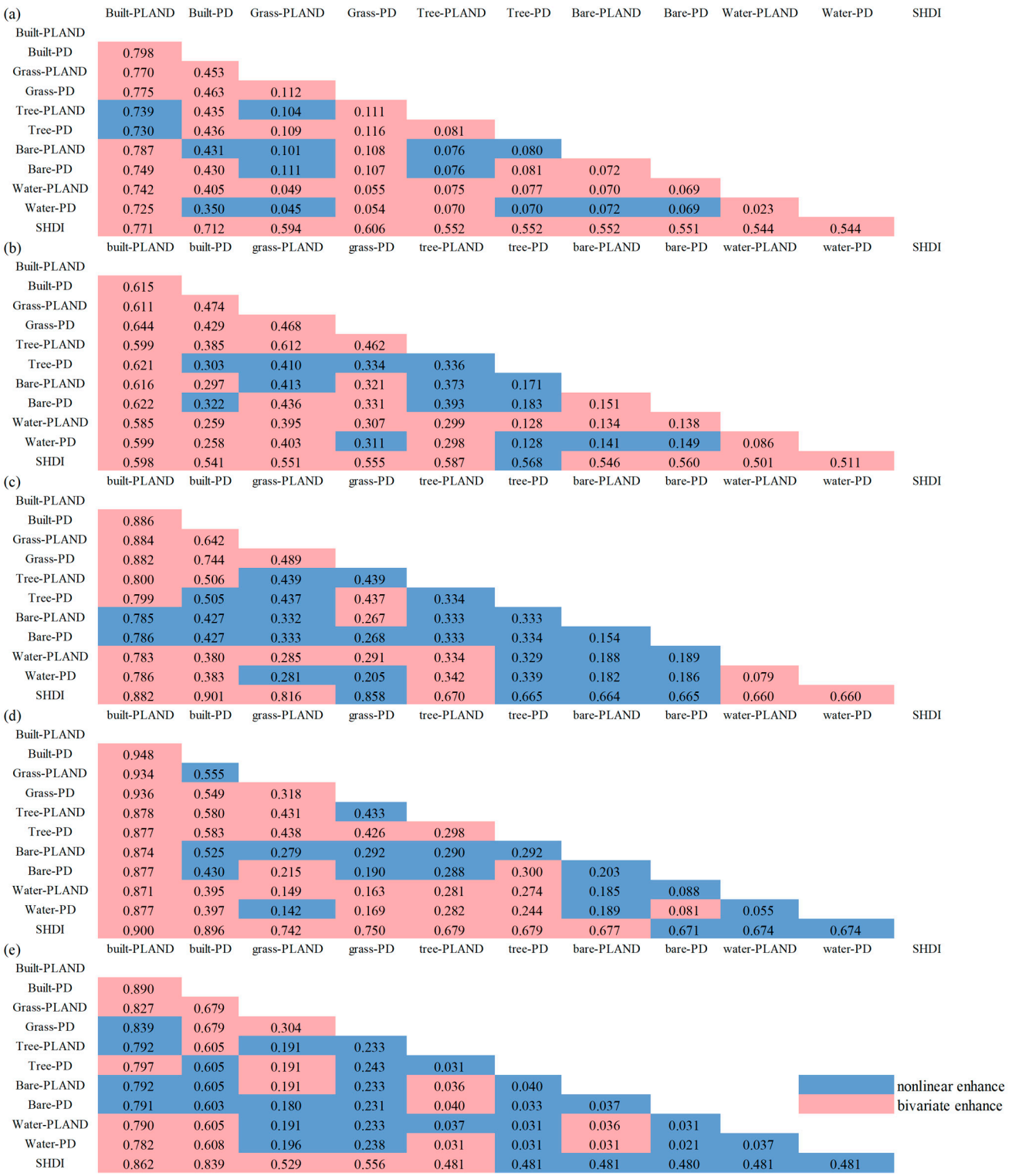

Figure 13. Two-dimensional factor interaction detection results in UFZs ((**a**) residential zone; (**b**) commercial zone; (**c**) industrial zone; (**d**) green space; (**e**) public service zone).

In the residential zones, the highest interactive explanatory power is between the height variance and built-PLAND (q = 0.825), followed by the interaction between the shape index and built-PLAND (q = 0.822). For the commercial zones, the highest interactive explanatory power is between the shape index and built-PLAND (q = 0.663), followed by the interaction between the shape coefficient and built-PLAND (q = 0.644). In the industrial

zones, the highest interactive explanatory power is between density and built-PLAND (q = 0.926), followed by the interaction between the height variance and built-PLAND (q = 0.911). In the green spaces, the highest interactive explanatory power is between built-PLAND and built-PLAND (q = 0.973), followed by the interaction between the mean height and built-PLAND (q = 0.965). In the public service zones, the highest interactive explanatory power is between the shape coefficient and built-PLAND (q = 0.917), followed by the interaction between the mean height and built-PLAND (q = 0.913).

(a)

	Shape index	Density	Shape coefficient	Mean height	Height variance	SVF
Built-PLAND	0.822	0.781	0.801	0.818	0.825	0.815
Built-PD	0.501	0.699	0.503	0.591	0.565	0.595
Grass-PLAND	0.237	0.586	0.171	0.233	0.211	0.285
Grass-PD	0.241	0.581	0.173	0.258	0.205	0.316
Tree-PLAND	0.222	0.582	0.133	0.209	0.158	0.268
Tree-PD	0.226	0.582	0.138	0.209	0.159	0.264
Bare-PLAND	0.219	0.579	0.128	0.207	0.155	0.262
Bare-PD	0.218	0.579	0.128	0.207	0.156	0.261
Water-PLAND	0.182	0.541	0.093	0.180	0.127	0.241
Water-PD	0.186	0.544	0.094	0.176	0.122	0.246
SHDI	0.639	0.724	0.639	0.682	0.690	0.675

(b)

	Shape index	Density	Shape coefficient	Mean height	Height variance	SVF
Built-PLAND	0.663	0.626	0.644	0.639	0.595	0.582
Built-PD	0.387	0.451	0.287	0.284	0.265	0.309
Grass-PLAND	0.439	0.439	0.441	0.461	0.415	0.390
Grass-PD	0.356	0.419	0.356	0.354	0.331	0.310
Tree-PLAND	0.431	0.506	0.320	0.323	0.304	0.339
Tree-PD	0.259	0.384	0.201	0.147	0.127	0.119
Bare-PLAND	0.246	0.372	0.183	0.155	0.127	0.130
Bare-PD	0.265	0.382	0.203	0.193	0.150	0.154
Water-PLAND	0.236	0.346	0.147	0.130	0.101	0.116
Water-PD	0.240	0.357	0.128	0.140	0.099	0.115
SHDI	0.604	0.579	0.602	0.603	0.555	0.531

(c)

	Shape index	Density	Shape coefficient	Mean height	Height variance	SVF
Built-PLAND	0.895	0.926	0.899	0.909	0.911	0.892
Built-PD	0.650	0.812	0.645	0.731	0.698	0.762
Grass-PLAND	0.418	0.786	0.524	0.654	0.665	0.630
Grass-PD	0.594	0.769	0.704	0.724	0.716	0.731
Tree-PLAND	0.427	0.699	0.465	0.570	0.563	0.561
Tree-PD	0.421	0.697	0.466	0.569	0.558	0.560
Bare-PLAND	0.313	0.553	0.332	0.494	0.495	0.488
Bare-PD	0.314	0.536	0.332	0.494	0.495	0.489
Water-PLAND	0.212	0.547	0.275	0.487	0.452	0.483
Water-PD	0.214	0.544	0.280	0.483	0.458	0.469
SHDI	0.898	0.874	0.879	0.863	0.895	0.750

(d)

	Shape index	Density	Shape coefficient	Mean height	Height variance	SVF
Built-PLAND	0.961	0.955	0.956	0.965	0.973	0.947
Built-PD	0.604	0.689	0.749	0.778	0.727	0.693
Grass-PLAND	0.515	0.712	0.467	0.539	0.486	0.503
Grass-PD	0.549	0.724	0.484	0.552	0.412	0.583
Tree-PLAND	0.443	0.763	0.417	0.370	0.364	0.424
Tree-PD	0.446	0.759	0.427	0.371	0.357	0.419
Bare-PLAND	0.402	0.637	0.339	0.336	0.324	0.393
Bare-PD	0.340	0.498	0.266	0.309	0.283	0.349
Water-PLAND	0.322	0.456	0.242	0.305	0.285	0.353
Water-PD	0.321	0.462	0.240	0.304	0.281	0.359
SHDI	0.858	0.906	0.892	0.873	0.872	0.776

(e)

	Shape index	Density	Shape coefficient	Mean height	Height variance	SVF
Built-PLAND	0.907	0.866	0.917	0.913	0.906	0.891
Built-PD	0.721	0.817	0.755	0.819	0.793	0.768
Grass-PLAND	0.403	0.569	0.410	0.384	0.297	0.355
Grass-PD	0.452	0.567	0.489	0.484	0.424	0.520
Tree-PLAND	0.281	0.471	0.243	0.176	0.149	0.200
Tree-PD	0.386	0.476	0.232	0.171	0.150	0.193
Bare-PLAND	0.286	0.479	0.204	0.177	0.149	0.200
Bare-PD	0.281	0.475	0.203	0.169	0.144	0.199
Water-PLAND	0.286	0.472	0.202	0.171	0.147	0.200
Water-PD	0.282	0.479	0.204	0.176	0.149	0.195
SHDI	0.653	0.784	0.670	0.842	0.853	0.818

nonlinear enhance
bivariate enhance

Figure 14. Two-dimensional/three-dimensional factor interaction detection results in UFZs ((**a**) residential zone; (**b**) commercial zone; (**c**) industrial zone; (**d**) green space; (**e**) public service zone).

In summary, from the perspective of the single-factor detection results, the spatial heterogeneity of LST in the UFZs within the Fifth Ring Road of Beijing is the result of the interaction and enhancement of multiple factors, rather than the independent action of a single factor. Single-factor detection can reflect the degree of influence of each factor on LST, while dual-factor interaction detection can better reveal the synergistic effects among various factors.

5. Discussion

5.1. Impact of 2D/3D Urban Morphology on LST

Previous research demonstrates that land use/cover is the most significant factor affecting the UHI. Agricultural fields and forests can effectively reduce urban temperatures, with the cooling effect dependent on the distribution and composition of these fields and forests [39]. While human activities significantly influence urban LST, these studies often overlook the impact of human activities on the urban heat environment, focusing more on 2D influencing factors. Therefore, this study explores the impact of UFZs resulting from human activities on the urban heat environment, as well as the differences in the impact of 2D and 3D urban morphology on the urban heat environment. The results show that residential zones have the highest LST, with the largest land area, industrial zones have the second-highest temperatures, and green spaces exhibit the lowest temperatures.

Some recent studies indicate a close relationship between building height and density in urban areas and LST, which is consistent with our findings. Additionally, other research highlights the significant regulatory role of urban tree, grass, and water bodies on LST, corroborating our conclusions.

Research indicates a strong positive correlation between building density and LST, while building height, shape index, and SVF show a negative correlation with LST. Similar findings have been noted in studies conducted in cities such as Beijing, Nanjing, and Seoul [15,40,41]. Previous research has also shown lower LST in areas with tall buildings, suggesting the influence of the urban canyon effect [41] and ventilation corridors [7,9]. High-rise buildings and roads create urban canyons, speeding up airflow over pavements. Moreover, buildings with simple shapes can more rapidly transfer heat carried in the air through urban areas, thereby slowing down the increase in LST. Deeper canyon spaces correspond to lower daytime LST [42]. Furthermore, high-rise areas provide more public spaces and ventilation corridors. Existing research indicates that a higher SVF represents a more expansive sky view, which aids in enhancing air circulation and wind speed in dense urban environments, thereby reducing temperature [43].

Research also indicates that grass, trees, and water have a significant impact on the variation of urban LST during summer days. Tree canopies create extensive shaded areas and reduce the absorption of solar radiation heat by transpiration, thereby lowering the LST [44]. Grass and water have a cooling effect through evaporation. When sunlight shines on grass and water surfaces, some water evaporates into water vapor, carrying away the surrounding heat and reducing the LST. Additionally, water has a high heat capacity, allowing it to absorb more heat without significant temperature rise, thereby reducing the rate of change in LST. Therefore, balancing the utilization of these elements in individual UFZs can maximize their cooling effects.

5.2. Comparison with Other Studies

A thorough examination of prior literature reveals that research on the factors impacting LST has predominantly investigated the correlation between LST and 2D/3D urban spatial morphology. This exploration has been conducted mainly from perspectives, such as overall societal activity space, urban clusters, cities, and regions. The findings demonstrate that the influential factors affecting LST vary, depending on the research scale. For instance, at the city scale, as observed in cities like Shijiazhuang, Xi'an, and Nanchang, the dominant factor influencing LST is the bare soil index (BSI) [45]. At the grid scale, the dominant factor for LST in the Seoul region is building height [46]. In this study, focusing on the scale of UFZs, the results indicate that within Beijing, the primary factors affecting urban LST in 2D urban morphology indicators are built-PLAND and SHDI, while in 3D urban morphology factors such as density, SVF, and shape index play a dominant role.

From the perspective of UFZs, our study reveals that the impact of the shape index is more pronounced compared to the study conducted by Huang et al. on the influence of 2D/3D UFZs on LST in Wuhan [20]. In our study, the shape index emerges as the primary influencing factor among urban 3D morphology parameters, leading us to conclude that simpler building shapes are more conducive to mitigating the urban heat island effect. Unlike Huang et al., who suggest that MH and SVF have a greater impact among 3D urban morphology parameters, our study indicates that the SVF and the shape index have a greater influence. Beijing features denser urban buildings compared to Wuhan, contributing to the higher impact of the shape index [47]. This regional disparity further demonstrates the complex mechanisms of urban microclimates at a fine scale and underscores the significance of our study for urban planning in cities similar to Beijing.

5.3. Limitations

This study has certain limitations that require further discussion. First, since the Landsat-8 data utilized in this study were obtained during daytime, nocturnal LST variations were not accounted for. Given the divergent temperature patterns between urban

day and night, particularly in narrow urban streets, this discrepancy might yield slightly different outcomes. Therefore, in future research, the utilization of MODIS day-night thermal data could be employed to explore the nocturnal relationship between urban morphology and LST. Second, despite efforts to correct errors in using the OSM road data for dividing Beijing's UFZs, potential omissions and errors may still exist during the manual identification process. Moreover, irregular research units may lead to the loss of edge details compared to regular grid or image elements. To achieve higher-precision UFZ mapping, future research could utilize more high-quality, open-source datasets and employ precise functional zone delineation from government departments. Finally, this study only explores the relationship between summer LST and UFZs in Beijing. Due to variations in human activities and solar radiation at different times, future research can investigate the spatial distribution of LST between different seasons and its influencing factors. In addition, we will consider introducing machine learning models to explore the relationship between 2D and 3D urban morphology and LST in the future. For instance, we may utilize the XGBoost model to establish the relationship between 2D and 3D urban morphology and LST, and employ the Shapley Additive exPlanation model to interpret the results [48].

5.4. Urban Planning Recommendations

Research shows that both 2D and 3D urban morphology parameters have a significant impact on LST in summer. Urban planning should focus on the distribution of buildings, grass, trees, and water. Buildings play a crucial role in LST by influencing solar radiation absorption, airflow, and anthropogenic heat release. Urban planners should aim to reduce building density and incorporate more trees, grasslands, and water bodies to alleviate the UHI effect. However, reducing artificial ground cover in land-constrained cities may not be feasible. Therefore, simplifying the shapes of buildings and raising building height can help reduce LST. Moreover, green spaces, trees, and water bodies can mitigate the UHI effect. In areas with limited green spaces, introducing these elements may be an effective approach to combating the UHI.

For UFZs, this study reveals the LST characteristics of different urban land use types, providing references for targeted landscape optimization and land-use planning to mitigate the environmental impact of urbanization. For instance, in high-density and high-rise residential zones, greater emphasis should be placed on the 3D design of buildings. In addition to focusing on the 3D design of buildings, residential zones should also consider the density and dispersed distribution of trees. Public service zones should prioritize increasing lawn coverage and adopting dispersed layouts. Industrial zones and green space zones should minimize variations in building heights to alleviate the LST within UFZs.

6. Conclusions

This study aimed to explore the impact of urban morphology on variations in urban LST, encompassing both 2D and 3D urban morphology. It employed Landsat-8 remote sensing data to retrieve LST, it utilized OSM road network data to delineate basic urban units, and combined multiple data sources with POI data for unsupervised and supervised functional zone identification. This study unraveled the intricate relationship between urban morphology and LST at the scale of UFZs. The analysis revealed the following key findings:

1. The LST in Beijing within the Fifth Ring Road exhibits an overall pattern of "higher in the center, lower in the periphery". Residential zones have the highest LST, followed by industrial zones. Notably, the public service zones show the highest standard deviation (0.95 °C), while the residential zones have the lowest (0.87 °C).
2. Significant correlations exist between LST and both 2D and 3D urban morphology parameters. GeoDetector results indicate that built-PLAND and SHDI are the primary factors influencing LST in 2D urban morphology, while density, SVF, and shape index play a major role in 3D urban morphology. Three-dimensional urban morphology,

including density, SVF, and shape index, also influences the variation of LST. Daytime LST tends to increase with building density, becoming higher as the complexity of building shapes increases. The SVF regulates ventilation, incoming solar radiation, and captures thermal radiation simultaneously, affecting LST. Therefore, it is advisable to reduce building density, increase building height, simplify building shapes, and disperse buildings. Additionally, the spatial distribution of trees, grasslands, and water bodies also helps mitigate LST, suggesting the adoption of fragmented distributions.

3. In interaction detection results, all UFZs exhibit the highest interaction with the built-PLAND factor, with q-values as follows: residential zones (0.825), commercial zones (0.663), industrial zones (0.926), green space (0.973), and public service zones (0.917). This underscores the dominant role of built-up areas in influencing urban LST.
4. Spatial variations are observed in the impact of different UFZs on LST. For instance, in residential, industrial, green space, and public service zones, the SVF is negatively correlated with LST, while in commercial zones, the SVF exhibits a positive correlation with LST. Additionally, in industrial zones and green space zones, height variance is positively correlated with LST, whereas in other UFZs, height variance shows a negative correlation with LST, with industrial zones and green space zones exhibiting a greater impact than the other three UFZs.

The forthcoming research will primarily focus on two aspects. First, it will investigate the relationship between UFZs and LST during different seasons, exploring whether influencing factors undergo changes. Second, recognizing potential variations in LST across diverse spatial scales, the study will investigate the impacts of different spatial scales on LST.

Author Contributions: Conceptualization, Shouhang Du; data curation, Yuhui Wu and Liyuan Guo; formal analysis, Yuhui Wu and Deqin Fan; funding acquisition, Shouhang Du; investigation, Shouhang Du; methodology, Shouhang Du, Yuhui Wu, and Liyuan Guo; resources, Deqin Fan and Wenbin Sun; software, Yuhui Wu; supervision, Shouhang Du and Yuhui Wu; validation, Shouhang Du, Yuhui Wu, Liyuan Guo, Deqin Fan, and Wenbin Sun; visualization, Yuhui Wu and Liyuan Guo; writing—original draft, Shouhang Du and Yuhui Wu. All authors have read and agreed to the published version of the manuscript.

Funding: This work was supported by the National Natural Science Foundation of China [42201512]; the China Postdoctoral Science Foundation [2021M703511; 2023T160691].

Data Availability Statement: Data will be made available on request.

Conflicts of Interest: No potential conflicts of interest were reported by the authors.

Abbreviations

Abbreviation	Full name
2D	Two-dimensional
3D	Three-dimensional
LST	Land surface temperature
UHI	Urban heat island
SUHI	Surface urban heat island
UHZs	Urban functional zones
OLI	Operational land imager
POI	Points of interest
OSM	OpenStreetMap
NDVI	Normalized difference vegetation index
NDWI	Normalized difference water index
OA	Overall accuracy
SHDI	Shannon's diversity index
PLAND	Percentage of landscape
PD	Patch density
Shape index	Area-weighted mean shape index
SVF	Sky view factor

References

1. Zhang, Z.; Luan, W.; Yang, J.; Guo, A.; Su, M.; Tian, C. The influences of 2D/3D urban morphology on land surface temperature at the block scale in Chinese megacities. *Urban Clim.* **2023**, *49*, 101553. [CrossRef]
2. Khoshnoodmotlagh, S.; Daneshi, A.; Gharari, S.; Verrelst, J.; Mirzaei, M.; Omrani, H. Urban morphology detection and it's linking with land surface temperature: A case study for Tehran Metropolis, Iran. *Sustain. Cities Soc.* **2021**, *74*, 103228. [CrossRef] [PubMed]
3. Lai, D.; Lian, Z.; Liu, W.; Guo, C.; Liu, W.; Liu, K.; Chen, Q. A comprehensive review of thermal comfort studies in urban open spaces. *Sci. Total. Environ.* **2020**, *742*, 140092. [CrossRef] [PubMed]
4. Oke, T.R.; Mills, G.; Christen, A.; Voogt, J.A. *Urban Climates*; Cambridge University Press: Cambridge, UK, 2017.
5. Liu, X.; Zhou, Y.; Yue, W.; Li, X.; Liu, Y.; Lu, D. Spatiotemporal patterns of summer urban heat island in Beijing, China using an improved land surface temperature. *J. Clean. Prod.* **2020**, *257*, 120529. [CrossRef]
6. Yang, J.; Jin, S.; Xiao, X.; Jin, C.; Xia, J.; Li, X.; Wang, S. Local climate zone ventilation and urban land surface temperatures: Towards a performance-based and wind-sensitive planning proposal in megacities. *Sustain. Cities Soc.* **2019**, *47*, 101487. [CrossRef]
7. Hidalgo-García, D.; Arco-Díaz, J. Modeling the Surface Urban Heat Island (SUHI) to study of its relationship with variations in the thermal field and with the indices of land use in the metropolitan area of Granada (Spain). *Sustain. Cities Soc.* **2022**, *87*, 104166. [CrossRef]
8. Peng, X.; Zhou, Y.; Fu, X.; Xu, J. Study on the spatial-temporal pattern and evolution of surface urban heat island in 180 shrinking cities in China. *Sustain. Cities Soc.* **2022**, *84*, 104018. [CrossRef]
9. Tran, D.X.; Pla, F.; Latorre-Carmona, P.; Myint, S.W.; Caetano, M.; Kieu, H.V. Characterizing the relationship between land use land cover change and land surface temperature. *ISPRS J. Photogramm. Remote Sens.* **2017**, *124*, 119–132. [CrossRef]
10. Yang, Q.; Huang, X.; Li, J. Assessing the relationship between surface urban heat islands and landscape patterns across climatic zones in China. *Sci. Rep.* **2017**, *7*, 9337. [CrossRef] [PubMed]
11. Azhdari, A.; Soltani, A.; Alidadi, M. Urban morphology and landscape structure effect on land surface temperature: Evidence from Shiraz, a semi-arid city. *Sustain. Cities Soc.* **2018**, *41*, 853–864. [CrossRef]
12. Bartesaghi-Koc, C.; Osmond, P.; Peters, A. Quantifying the seasonal cooling capacity of 'green infrastructure types' (GITs): An approach to assess and mitigate surface urban heat island in Sydney, Australia. *Landsc. Urban Plan.* **2020**, *203*, 103893. [CrossRef]
13. Logan, T.M.; Zaitchik, B.; Guikema, S.; Nisbet, A. Night and day: The influence and relative importance of urban characteristics on remotely sensed land surface temperature. *Remote Sens. Environ.* **2020**, *247*, 111861. [CrossRef]
14. Dai, Z.; Guldmann, J.-M.; Hu, Y. Spatial regression models of park and land-use impacts on the urban heat island in central Beijing. *Sci. Total. Environ.* **2018**, *626*, 1136–1147. [CrossRef] [PubMed]
15. Yin, S.; Liu, J.; Han, Z. Relationship between urban morphology and land surface temperature—A case study of Nanjing City. *PLoS ONE* **2022**, *17*, e0260205. [CrossRef] [PubMed]
16. Futcher, J.; Mills, G.; Emmanuel, R.; Korolija, I. Creating sustainable cities one building at a time: Towards an integrated urban design framework. *Cities* **2017**, *66*, 63–71. [CrossRef]
17. Guo, A.; Yue, W.; Yang, J.; He, T.; Zhang, M.; Li, M. Divergent impact of urban 2D/3D morphology on thermal environment along urban gradients. *Urban Clim.* **2022**, *45*, 101278. [CrossRef]
18. Li, H.; Li, Y.; Wang, T.; Wang, Z.; Gao, M.; Shen, H. Quantifying 3D building form effects on urban land surface temperature and modeling seasonal correlation patterns. *Build. Environ.* **2021**, *204*, 108132. [CrossRef]
19. Alavipanah, S.; Schreyer, J.; Haase, D.; Lakes, T.; Qureshi, S. The effect of multi-dimensional indicators on urban thermal conditions. *J. Clean. Prod.* **2018**, *177*, 115–123. [CrossRef]
20. Huang, X.; Wang, Y. Investigating the effects of 3D urban morphology on the surface urban heat island effect in urban functional zones by using high-resolution remote sensing data: A case study of Wuhan, Central China. *ISPRS J. Photogramm. Remote Sens.* **2019**, *152*, 119–131. [CrossRef]
21. Koko, A.F.; Yue, W.; Abubakar, G.A.; Alabsi, A.A.N.; Hamed, R. Spatiotemporal Influence of Land Use/Land Cover Change Dynamics on Surface Urban Heat Island: A Case Study of Abuja Metropolis, Nigeria. *ISPRS Int. J. Geo-Inf.* **2021**, *10*, 272. [CrossRef]
22. Chen, Y.; Yang, J.; Yu, W.; Ren, J.; Xiao, X.; Xia, J.C. Relationship between urban spatial form and seasonal land surface temperature under different grid scales. *Sustain. Cities Soc.* **2023**, *89*, 104374. [CrossRef]
23. Bateman, I.J.; Harwood, A.R.; Mace, G.M.; Watson, R.T.; Abson, D.J.; Andrews, B.; Binner, A.; Crowe, A.; Day, B.H.; Dugdale, S.; et al. Bringing ecosystem services into economic decision-making: Land use in the United Kingdom. *Science* **2013**, *341*, 45–50. [CrossRef] [PubMed]
24. National Bureau of Statistics of China. *Chinese Statistics Summary 2023*; China Statistics Press: Beijing, China, 2023.
25. Jiang, W.; He, G.; Long, T.; Guo, H.; Yin, R.; Leng, W.; Liu, H.; Wang, G. Potentiality of Using Luojia 1-01 Nighttime Light Imagery to Investigate Artificial Light Pollution. *Sensors* **2018**, *18*, 2900. [CrossRef] [PubMed]
26. Lu, P.; Shi, W.; Wang, Q.; Li, Z.; Qin, Y.; Fan, X. Co-seismic landslide mapping using Sentinel-2 10-m fused NIR narrow, red-edge, and SWIR bands. *Landslides* **2021**, *18*, 2017–2037. [CrossRef]
27. Hong, Y.; Yao, Y. Hierarchical community detection and functional area identification with OSM roads and complex graph theory. *Int. J. Geogr. Inf. Sci.* **2019**, *33*, 1569–1587. [CrossRef]

28. Lemus-Canovas, M.; Martin-Vide, J.; Moreno-Garcia, M.C.; Lopez-Bustins, J.A. Estimating Barcelona's metropolitan daytime hot and cold poles using Landsat-8 Land Surface Temperature. *Sci. Total. Environ.* **2020**, *699*, 134307. [CrossRef] [PubMed]
29. Ke, X.; Men, H.; Zhou, T.; Li, Z.; Zhu, F. Variance of the impact of urban green space on the urban heat island effect among different urban functional zones: A case study in Wuhan. *Urban For. Urban Green.* **2021**, *62*, 127159. [CrossRef]
30. Feng, Y.; Du, S.; Myint, S.W.; Shu, M. Do Urban Functional Zones Affect Land Surface Temperature Differently? A Case Study of Beijing, China. *Remote Sens.* **2019**, *11*, 1802. [CrossRef]
31. Hu, T.; Yang, J.; Li, X.; Gong, P. Mapping Urban Land Use by Using Landsat Images and Open Social Data. *Remote Sens.* **2016**, *8*, 151. [CrossRef]
32. Breiman, L. Randomizing outputs to increase prediction accuracy. *Mach. Learn.* **2000**, *40*, 229–242. [CrossRef]
33. Knotters, M.; Brus, D.J. Purposive versus random sampling for map validation: A case study on ecotope maps of floodplains in the Netherlands. *Ecohydrology* **2013**, *6*, 425–434. [CrossRef]
34. Wang, P.; Yu, Q.; Pei, Y.; Wang, G.; Yue, D.; Hou, H. Scale Effect Analysis of Landscape Pattern in Wengniute Banner. *Trans. Agric. Mach.* **2020**, *51*, 223–231+181.
35. Wu, Z.; Hou, Q.; Yang, Z.; Yu, T.; Li, D.; Lin, K.; Ma, X. Identification of factors driving the spatial distribution of molybdenum (Mo) in topsoil in the Longitudinal Range-Gorge Region of Southwestern China using the Geodetector model. *Ecotoxicol. Environ. Saf.* **2024**, *271*, 115846. [CrossRef]
36. Rauf, S.; Pasra, M.M.; Yuliani. Analysis of correlation between urban heat islands (UHI) with land-use using sentinel 2 time-series image in Makassar city. *IOP Conf. Ser. Earth Environ. Sci.* **2020**, *419*, 012088. [CrossRef]
37. Wang, J.; Xu, C. Geodetector: Principle and prospective. *J. Geogr. Sci.* **2017**, *72*, 116–134.
38. Chen, Y.; Wu, J. Research on the Spatial Pattern and Influencing Factors of TourismComponents in Xi'an Based on POI Data. *Surv. Geogr. Inf.* **2023**, *48*, 96–100. [CrossRef]
39. Wang, R.; Hou, H.; Murayama, Y.; Derdouri, A. Spatiotemporal Analysis of Land Use/Cover Patterns and Their Relationship with Land Surface Temperature in Nanjing, China. *Remote Sens.* **2020**, *12*, 440. [CrossRef]
40. Zheng, Z.; Zhou, W.; Yan, J.; Qian, Y.; Wang, J.; Li, W. The higher, the cooler? Effects of building height on land surface temperatures in residential areas of Beijing. *Phys. Chem. Earth Parts A/B/C* **2019**, *110*, 149–156. [CrossRef]
41. Kim, E.-S.; Yun, S.-H.; Park, C.-Y.; Heo, H.-K.; Lee, D.-K. Estimation of Mean Radiant Temperature in Urban Canyons Using Google Street View: A Case Study on Seoul. *Remote Sens.* **2022**, *14*, 260. [CrossRef]
42. Luo, P.; Yu, B.; Li, P.; Liang, P.; Liang, Y.; Yang, L. How 2D and 3D built environments impact urban surface temperature under extreme heat: A study in Chengdu, China. *Build. Environ.* **2023**, *231*, 110035. [CrossRef]
43. Yang, F.; Qian, F.; Lau, S.S.Y. Urban form and density as indicators for summertime outdoor ventilation potential: A case study on high-rise housing in Shanghai. *Build. Environ.* **2013**, *70*, 122–137. [CrossRef]
44. Huang, J.; Wang, Y. Cooling intensity of hybrid landscapes in a metropolitan area: Relative contribution and marginal effect. *Sustain. Cities Soc.* **2022**, *79*, 103725. [CrossRef]
45. Wang, Y.; Yi, G.; Zhou, X.; Zhang, T.; Bie, X.; Li, J.; Ji, B. Spatial distribution and influencing factors on urban land surface temperature of twelve megacities in China from 2000 to 2017. *Ecol. Indic.* **2021**, *125*, 107533. [CrossRef]
46. Jeon, G.; Park, Y.; Guldmann, J.-M. Impacts of Urban Morphology on Seasonal Land Surface Temperatures: Comparing Grid- and Block-Based Approaches. *ISPRS Int. J. Geo-Inf.* **2023**, *12*, 482. [CrossRef]
47. Cai, Z.; Tang, Y.; Liu, C.; Demuzere, M. Analyzing the Transformation of 3D Urban Morphology and Corresponding Surface Heat Island Effect in Beijing. *Urban Plan. Int.* **2021**, *36*, 61–68. [CrossRef]
48. Zhi, D.; Zhao, H.; Chen, Y.; Song, W.; Song, D.; Yang, Y. Quantifying the heterogeneous impacts of the urban built environment on traffic carbon emissions: New insights from machine learning techniques. *Urban Clim.* **2024**, *53*, 101765. [CrossRef]